submitted to *Geophys. J. Int.*

Magnetic radial inversion for 3-D source geometry estimation

L.B. Vital[1⋆], V.C. Oliveira Jr.[1] and V.C.F. Barbosa[1]

[1] *Observatório Nacional, Gal. José Cristino, 77, São Cristóvão, Rio de Janeiro, 20921-400, Brazil*

SUMMARY

We present a method for inverting total-field anomaly data to estimate the geometry of a uniformly magnetized 3-D geological source in the subsurface. The method assumes the total-magnetization direction is known. We approximate the source by an ensemble of vertically juxtaposed right prisms, all of them with the same total-magnetization vector and depth extent. The horizontal cross-section of each prism is defined by a polygon having the same number of vertices equally spaced from $0°$ to $360°$, whose polygon vertices are described by polar coordinates with an origin defined by a horizontal location over the top of each prism. Because our method estimates the radii of each polygon vertex we refer to it as *radial inversion*. The position of these vertices, the horizontal location of each prism and the depth extent of all prisms are the parameters to be estimated by solving a constrained nonlinear inverse problem of minimizing a goal function. We run successive inversions for a range of tentative total-magnetization intensities and depths to the top of the shallowest prism. The estimated models producing the lowest values of the goal function form the set of candidate solutions. To obtain stabilized solutions, we impose the zeroth- and first-order Tikhonov regularizations on the shape of the prisms. The method allows estimating the geometry of both vertical and inclined sources, with a constant direction of magnetization, by using the Tikhonov regularization. Tests with synthetic data show that the method can be of utility in estimating the shape of the magnetic source even in the presence of a strong regional field. Results obtained by inverting airborne total-field anomaly data over the Anitápolis alkaline-carbonatitic complex, in southern Brazil, suggest that the emplacement of the magnetic sources was controlled by NW-SE-trending faults at depth, in accordance with known structural features at the study area.

Key words: Magnetic anomalies: modelling and interpretation; Inverse theory; Numerical solutions.

⋆ leobvital@gmail.com

1 INTRODUCTION

The interpretation of total-field anomalies on the surface of the Earth is an important challenge in exploration geophysics due to the nonuniqueness of 3-D magnetic inversion. It is well-known that several magnetization distributions in subsurface can reproduce the same magnetic data with the same accuracy. To overcome this inherent ambiguity, a priori information needs to be introduced for reducing the number of possible solutions that are coherent with the local geology. The available a priori information determines the suitable inverse method to be applied. As explained below, we identified, in the literature, three groups of 3-D magnetic inversion methods.

The first group of inverse methods approximates the source by a geometrically simple causative body having its geometry defined by a small number of parameters (e.g., Ballantyne 1980; Bhattacharyya 1980; Silva & Hohmann 1983). These methods estimate both the geometry and the physical property of the source by solving a nonlinear inverse problem. Due to the very restrictive parametrization, such methods usually do not have severe problems with ambiguity.

The second group of inverse methods is formed by the vast majority of methods. These methods approximate the subsurface by a grid of juxtaposed rectangular prisms having a constant total-magnetization direction. Some methods presume that a purely induced magnetization and the isotropic magnetic susceptibility of the prisms is the quantity estimated by solving a linear inverse problem. Some examples of this linear inversion are presented by Cribb (1976), Li & Oldenburg (1996) and Pilkington (1997). Different approaches have improved this linear inversion to obtain focused images of the subsurface. For example, Portniaguine & Zhdanov (1999) and Portniaguine & Zhdanov (2002) introduced the minimum gradient support functional, similar to the one proposed by Last & Kubik (1983) that minimizes the volumes of the sources in a gravity data inversion. By inverting magnetic anomaly and any component of the total anomalous field, this functional estimates a magnetization distribution that generates a non blurry (focused) 3-D image of the geologic bodies in the subsurface. Barbosa & Silva (2006) presented a method for inverting interfering magnetic anomalies produced by multiple sources by combining features of the forward modeling (the interactivity) and traditional inversion (the automatic data fitting). Other studies introduced strategies to constraint the nonuniqueness and delineate the source (Caratori Tontini et al. 2006; Pilkington 2009; Shamsipour et al. 2011; Cella & Fedi 2012; Abedi et al. 2015). Some of these methods allowed remanent magnetization (e.g., Pignatelli et al. 2006). In this case, the parameters to be estimated are the total-magnetization intensities of the prisms. In all these methods, and thus, the geometries of the magnetic sources are indirectly retrived by interpreting the estimated total-magnetization intensity distribution. Theoretically, these inversion methods are capable of recovering the geometry of complex sources. However, they require a plethora of a priori information to overcome their nonuniqueness and instability due to the large number of parameters to be estimated. Additionally, they are characterized by a high computational cost associated with the solution of large linear systems.

The third group of 3-D magnetic inversion methods requires some knowledge about the physical property distribution to estimate the geometry of the sources. They are usually formulated as nonlinear inverse problems. Wang & Hansen (1990) approximated the source by a polyhedron and estimate the position of its vertices in the Fourier domain. Li et al. (2017) developed a multiple level-set method to estimate geometry of a set of causative bodies with uniform magnetic susceptibility. Hidalgo-Gato & Barbosa (2019) inverted the total-field anomaly for estimating the depths to the top of a magnetic basement of a sedimentary basin with known magnetization intensity but unknown magnetization direction. An inverse method in this third group has a small number of parameters to be estimated by inversion and has much less ambiguity in comparison to the second group.

By following the third group of 3-D magnetic inversion methods, we present a magnetic inversion to estimate the geometry of an isolated and uniformly magnetized 3-D source with known total-magnetization direction. Our method is an extension of the methods presented by Oliveira Jr. et al. (2011) and Oliveira Jr. & Barbosa (2013) for inverting, respectively, gravity and gravity-gradient data, applied to the total-field anomaly. We approximate the source by a stack of vertically juxtaposed right prisms with polygonal horizontal cross-sections and the same number of vertices. For convenience, all prisms have the same thickness and total-magnetization intensity. Differently from Oliveira Jr. et al. (2011) and Oliveira Jr. & Barbosa (2013), our method estimates not only the horizontal Cartesian coordinates of the origins and the radii of the vertices describing the horizontal cross-sections of all prisms, but also the thickness of all prisms comprising the interpretation model. Additionally, we perform a numerical analysis to investigate the sensitivity of our method to the key inversion parameters, namely, the total magnetization intensity and the depth to the top of the shallowest prism. We perform a series of inversion runs using different combinations of these two parameters' values and compute a goal function associated with each of the trial solutions. Among the estimated models, those producing the lowest values of goal function form the set of candidate models. To obtain a stable solutions, we use the same set of regularizing functions proposed by Oliveira Jr. et al. (2011) and also propose a new one for constraining the thickness of the prisms. Like Oliveira Jr. et al. (2011) and Oliveira Jr. & Barbosa (2013), we refer to the proposed method as *radial inversion* because our method estimates the radii of the vertices describing the horizontal cross-sections of all prisms. Tests on synthetic data and on airborne magnetic data collected over the alkaline-carbonatitic complex of Anitápolis, in southern Brazil, show the potential of our method in retrieving 3-D magnetic bodies even if they exhibit variable shapes in depth.

2 METHODOLOGY

2.1 Forward problem

Let $\mathbf{d}^o$ be the observed data vector, whose ith element d_i^o, $i = 1, \ldots, N$, is the total-field anomaly produced by a 3-D source (Fig. 1a) at the point (x_i, y_i, z_i) of a Cartesian coordinate system with x, y and z axes pointing to north, east and down, respectively. We assume that the direction of the total magnetization vector of the source is constant and known. We approximate the volume of the source by a set of L vertically juxtaposed 3-D prisms (Fig. 1b) by following the same approach of Oliveira Jr. et al. (2011) and Oliveira Jr. & Barbosa (2013). The depth to the top of the shallowest prism is defined by z_0 and m_0 is the constant total-magnetization intensity of all prisms. The horizontal cross-section of each prism (Fig. 2) is described by a polygon with a fixed number V of vertices equally spaced from $0°$ to $360°$, which are described in polar coordinates referred to an internal origin O^k. The radii of the vertices (r_j^k, $j = 1, \ldots, V$, $k = 1, \ldots, L$), the horizontal coordinates (x_0^k and y_0^k, $k = 1, \ldots, L$) of the origins O^k, $k = 1, \ldots, L$, and the thickness dz of the L vertically stacked prisms (Fig. 1b) are arranged in a $M \times 1$ parameter vector $\mathbf{p}$, $M = L(V + 2) + 1$, given by

$$\mathbf{p} = \begin{bmatrix} \mathbf{r}^{1\mathsf{T}} & x_0^1 & y_0^1 & \ldots & \mathbf{r}^{L\mathsf{T}} & x_0^L & y_0^L & dz \end{bmatrix}^{\mathsf{T}}, \tag{1}$$

where "T" denotes transposition and $\mathbf{r}^k$ is a $V \times 1$ vector containing the radii r_j^k of the kth prism. Let $\mathbf{d}(\mathbf{p})$ be the predicted data vector, whose ith element

$$d_i(\mathbf{p}) \equiv \sum_{k=1}^{L} f_i^k(\mathbf{r}^k, x_0^k, y_0^k, dz, z_1^k, m_0), \quad i = 1, \ldots, N, \tag{2}$$

is the total-field anomaly produced by the ensemble of L prisms at the ith observation point (x_i, y_i, z_i). In eq. 2, $f_i^k(\mathbf{r}^k, x_0^k, y_0^k, dz, z_1^k, m_0)$ is the total-field anomaly produced, at the observation point (x_i, y_i, z_i), by the kth prism, with depth to the top $z_1^k = z_0 + (k-1)dz$. We calculate $d_i(\mathbf{p})$ (eq. 2) by using the Python package Fatiando a Terra (Uieda et al. 2013), which implements the formulas proposed by Plouff (1976).

It is noteworthy that eq. (2) can be rewritten as

$$d_i(\mathbf{p}) \equiv m_0 \sum_{k=1}^{L} f_i^k(\mathbf{r}^k, x_0^k, y_0^k, dz, z_1^k, 1), \quad i = 1, \ldots, N, \tag{3}$$

because there is a linear relationship between the predicted data $\mathbf{d}(\mathbf{p})$ and the total-magnetization intensity m_0. In eq. (3) the function $f_i^k(\mathbf{r}^k, x_0^k, y_0^k, dz, z_1^k, 1)$ is numerically equal to the total-field anomaly produced by the kth prism, with unitary magnetization intensity at the ith observation position.

2.2 Inverse problem formulation

Given a set of tentative values for the total-magnetization intensity m_0 and depth to the top of the shallowest prism z_0, we solve a constrained non-linear problem to estimate the parameter vector $\mathbf{p}$ (eq. 1) by minimizing the goal function

$$\Gamma(\mathbf{p}) = \phi(\mathbf{p}) + \sum_{\ell=1}^{7} \alpha_\ell \, \varphi_\ell(\mathbf{p}) \, , \tag{4}$$

subject to

$$p_l^{min} < p_l < p_l^{max}, \quad l = 1, \ldots, M \, , \tag{5}$$

where $\phi(\mathbf{p})$ is the data-misfit function given by

$$\phi(\mathbf{p}) = \frac{1}{N} \| \mathbf{d}^o - \mathbf{d}(\mathbf{p}) \|_2^2 \, , \tag{6}$$

which represents the normalized squared Euclidean norm of the difference between the observed $\mathbf{d}^o$ and predicted $\mathbf{d}(\mathbf{p})$ data vector.

The second term in the right side of eq. (4) represents the weighted sum of the seven constraint functions $\varphi_\ell(\mathbf{p})$, $\ell = 1, \ldots, 7$ described in the subsection *Constraint functions* later in this article. In eq. (4), α_ℓ is a positive number representing the weight of the ℓth constraint function $\varphi_\ell(\mathbf{p})$. These weights α_ℓ will be rescaled and selected according to a criterion described in the subsection *Computational procedures* later in this article. In the inequality constraints (5) p_l^{min} and p_l^{max} are, respectively, the lower and upper limits for the lth element p_l of the parameter vector $\mathbf{p}$ (eq. 1). These limits are defined by the interpreter based on both the horizontal extent of the magnetic anomaly and the knowledge about the source. On the discrete mapping of the goal function $\Gamma(\mathbf{p})$ (eq. 4) obtained by using each previously defined pair (m_0, z_0), we select the optimum values of m_0 and z_0 as those producing the smallest value of the goal function $\Gamma(\mathbf{p})$.

To solve our nonlinear inverse problem for each pair of total-magnetization intensity m_0 and depth to the top of the shallowest prism z_0, we use a gradient-based method and, consequently, we need to define the gradient vector $\boldsymbol{\nabla}\Gamma(\mathbf{p})$ and Hessian matrix $\mathbf{H}(\mathbf{p})$ of the goal function $\Gamma(\mathbf{p})$ (eq. 4):

$$\boldsymbol{\nabla}\Gamma(\mathbf{p}) = \boldsymbol{\nabla}\phi(\mathbf{p}) + \sum_{\ell=1}^{7} \alpha_\ell \, \boldsymbol{\nabla}\varphi_\ell(\mathbf{p}) \tag{7}$$

and

$$\mathbf{H}(\mathbf{p}) = \mathbf{H}_\phi(\mathbf{p}) + \sum_{\ell=1}^{7} \alpha_\ell \, \mathbf{H}_\ell \, , \tag{8}$$

where the gradient vector and the Hessian matrix of the misfit function $\phi(\mathbf{p})$ (eq. 4) are respectively given by:

$$\boldsymbol{\nabla}\phi(\mathbf{p}) = -\frac{2}{N}\mathbf{G}(\mathbf{p})^{\mathsf{T}}[\mathbf{d}^{o} - \mathbf{d}(\mathbf{p})] \tag{9}$$

and

$$\mathbf{H}_{\phi}(\mathbf{p}) = \frac{2}{N}\mathbf{G}(\mathbf{p})^{\mathsf{T}}\mathbf{G}(\mathbf{p}) \, . \tag{10}$$

In eqs. 7 and 8, the terms $\boldsymbol{\nabla}\varphi_{\ell}(\mathbf{p})$ and $\mathbf{H}_{\ell}$, $\ell = 1, \dots, 7$, are the gradient vectors and Hessian matrices of the constraint functions, respectively. In eqs. 9 and 10, $\mathbf{G}(\mathbf{p})$ is an $N \times M$ matrix whose element ij is the derivative of the predicted data $d_i(\mathbf{p})$ (eq. 2) with respect to the j element p_j of the parameter vector $\mathbf{p}$ (eq. 1). Details about the constraint functions $\varphi_{\ell}(\mathbf{p})$, $\ell = 1, \dots, 7$, as well as the numerical procedure to solve this nonlinear inverse problem are given in the following sections.

2.3 Constraint functions

To explain the constraint functions $\varphi_{\ell}(\mathbf{p})$ (eq. 4), $\ell = 1, \dots, 7$, used here to obtain stable solutions and introduce prior information about the magnetic source, we have organized them into the following three groups.

2.3.1 Smoothness constraints

This group is formed by variations of the first-order Tikhonov regularization (Aster et al. 2019, p. 103) that imposes smoothness on the radii r_j^k and the Cartesian coordinates x_0^k and y_0^k of the origin O^k, $j = 1, \dots, V$, $k = 1, \dots, L$, defining the horizontal section of each prism (Fig.1b). They were proposed by Oliveira Jr. et al. (2011) and Oliveira Jr. & Barbosa (2013) and play a very important role in introducing prior information about the shape of the source.

The first constraint of this group is the *smoothness constraint on the adjacent radii defining the horizontal section of each vertical prism*. This constraint imposes that adjacent radii r_j^k and r_{j+1}^k within each prism must be close to each other. It forces the estimated prism to be approximately cylindrical. Mathematically, the constraint is given by

$$\begin{aligned} \varphi_1(\mathbf{p}) &= \sum_{k=1}^{L} \left[\left(r_V^k - r_1^k \right)^2 + \sum_{j=1}^{V-1} \left(r_j^k - r_{j+1}^k \right)^2 \right] \\ &= \mathbf{p}^{\mathsf{T}}\mathbf{R}_1^{\mathsf{T}}\mathbf{R}_1\mathbf{p} \quad , \end{aligned} \tag{11}$$

where

$$\mathbf{R}_1 = \mathbf{I}_L \otimes \left[\left(\mathbf{I}_V - \mathbf{D}_V^{\mathsf{T}} \right) \quad \mathbf{0}_{V\times 2} \right]_{(LV\times M)} \quad , \tag{12}$$

$\mathbf{I}_L$ is the identity matrix of order L, "$\otimes$" denotes the Kronecker product (Horn & Johnson 1991, p. 243), $\mathbf{0}_{V\times 2}$ is a $V \times 2$ matrix with null elements, $\mathbf{I}_V$ is the identity matrix of order V and $\mathbf{D}_V^{\mathsf{T}}$ is the upshift permutation matrix of order V (Golub & Loan 2013, p. 20). The gradient and Hessian of function $\varphi_1(\mathbf{p})$ (eq. 11) are given by:

$$\boldsymbol{\nabla}\varphi_1(\mathbf{p}) = 2\mathbf{R}_1^{\mathsf{T}}\mathbf{R}_1\mathbf{p} \quad , \tag{13}$$

and

$$\mathbf{H}_1(\mathbf{p}) = 2\mathbf{R}_1^{\mathsf{T}}\mathbf{R}_1 \quad . \tag{14}$$

The second constraint of this group is the *smoothness constraint on the adjacent radii of the vertically adjacent prisms*, which imposes that adjacent radii r_j^k and r_j^{k+1} within vertically adjacent prisms must be close to each other. This constraint forces the shape of all prisms to be similar to each other and is given by

$$\begin{aligned} \varphi_2(\mathbf{p}) &= \sum_{k=1}^{L-1}\left[\sum_{j=1}^{V}\left(r_j^{k+1} - r_j^k\right)^2\right] \quad , \\ &= \mathbf{p}^{\mathsf{T}}\mathbf{R}_2^{\mathsf{T}}\mathbf{R}_2\mathbf{p} \end{aligned} \tag{15}$$

where

$$\mathbf{R}_2 = \begin{bmatrix}\mathbf{S}_2 & \mathbf{0}_{(L-1)V\times 1}\end{bmatrix}_{(L-1)V\times M} \quad , \tag{16}$$

$$\mathbf{S}_2 = \left(\begin{bmatrix}\mathbf{I}_{L-1} & \mathbf{0}_{(L-1)\times 1}\end{bmatrix} - \begin{bmatrix}\mathbf{0}_{(L-1)\times 1} & \mathbf{I}_{L-1}\end{bmatrix}\right) \otimes \begin{bmatrix}\mathbf{I}_V & \mathbf{0}_{V\times 2}\end{bmatrix} \quad , \tag{17}$$

$\mathbf{0}_{(L-1)V\times 1}$ is an $(L-1)V \times 1$ vector with null elements, $\mathbf{0}_{(L-1)\times 1}$ is an $(L-1)\times 1$ vector with null elements and $\mathbf{I}_{L-1}$ is the identity matrix of order $L-1$. The gradient and Hessian of function $\varphi_2(\mathbf{p})$ (eq. 15) are given by:

$$\boldsymbol{\nabla}\varphi_2(\mathbf{p}) = 2\mathbf{R}_2^{\mathsf{T}}\mathbf{R}_2\mathbf{p} \quad , \tag{18}$$

and

$$\mathbf{H}_2(\mathbf{p}) = 2\mathbf{R}_2^{\mathsf{T}}\mathbf{R}_2 \quad . \tag{19}$$

The last constraint of this group is the *smoothness constraint on the horizontal position of the arbitrary origins of the vertically adjacent prisms*. This constraint imposes that the estimated horizontal Cartesian coordinates (x_0^k, y_0^k) and (x_0^{k+1}, y_0^{k+1}) of the origins O^k and O^{k+1} of adjacent prisms must be close to each other. It forces the centers of the prisms to be vertically aligned. This constraint is given by

$$\begin{aligned} \varphi_3(\mathbf{p}) &= \sum_{k=1}^{L-1}\left[\left(x_0^{k+1} - x_0^k\right)^2 + \left(y_0^{k+1} - y_0^k\right)^2\right] \quad , \\ &= \mathbf{p}^{\mathsf{T}}\mathbf{R}_3^{\mathsf{T}}\mathbf{R}_3\mathbf{p} \end{aligned} \tag{20}$$

where

$$\mathbf{R}_3 = \begin{bmatrix} \mathbf{S}_3 & \mathbf{0}_{(L-1)2\times 1} \end{bmatrix}_{(L-1)2\times M} \quad , \tag{21}$$

$$\mathbf{S}_3 = \left(\begin{bmatrix} \mathbf{I}_{L-1} & \mathbf{0}_{(L-1)\times 1} \end{bmatrix} - \begin{bmatrix} \mathbf{0}_{(L-1)\times 1} & \mathbf{I}_{L-1} \end{bmatrix} \right) \otimes \begin{bmatrix} \mathbf{0}_{2\times V} & \mathbf{I}_2 \end{bmatrix} \quad , \tag{22}$$

$\mathbf{0}_{(L-1)2\times 1}$ is an $(L-1)2 \times 1$ vector with null elements, $\mathbf{0}_{2\times V}$ is a $2 \times V$ matrix with null elements and $\mathbf{I}_2$ is the identity matrix of order 2. The gradient and Hessian of function $\varphi_3(\mathbf{p})$ (eq. 20) are given by:

$$\boldsymbol{\nabla}\varphi_3(\mathbf{p}) = 2\mathbf{R}_3^\intercal \mathbf{R}_3 \mathbf{p} \quad , \tag{23}$$

and

$$\mathbf{H}_3(\mathbf{p}) = 2\mathbf{R}_3^\intercal \mathbf{R}_3 \quad . \tag{24}$$

2.3.2 Equality constraints

This group is formed by two constraints that were proposed by Oliveira Jr. et al. (2011) and Oliveira Jr. & Barbosa (2013) by following the same approach proposed Barbosa et al. (1997) and Barbosa et al. (1999a). They introduce a priori information about the shallowest prism and are suitable for outcropping sources.

The *source's outcrop constraint* imposes that the horizontal cross-section of the shallowest prism must be close to known outcropping boundary of the geologic source. The horizontal cross-section of the known outcropping boundary separating the geologic source from the host rock is described by the radii $\tilde{r}_1^0 \ldots \tilde{r}_V^0$. Mathematically, this constraint is given by

$$\begin{aligned} \varphi_4(\mathbf{p}) &= \left[\sum_{j=1}^{V} \left(r_j^1 - r_j^0 \right)^2 \right] \\ &= \left(\mathbf{R}_4\mathbf{p} - \mathbf{a} \right)^\intercal \left(\mathbf{R}_4\mathbf{p} - \mathbf{a} \right) \end{aligned} \quad , \tag{25}$$

where $\mathbf{a}$ is a $V \times 1$ vector containing the radii of the polygon defining the outcropping boundary

$$\mathbf{a} = \begin{bmatrix} \tilde{r}_1^0 & \ldots & \tilde{r}_V^0 \end{bmatrix}^\intercal , \tag{26}$$

and

$$\mathbf{R}_4 = \begin{bmatrix} \mathbf{I}_V & \mathbf{0}_{V\times(M-V)} \end{bmatrix}_{V\times M} , \tag{27}$$

where $\mathbf{I}_V$ is the identity matrix of order V and $\mathbf{0}_{V\times(M-V)}$ is a $V\times(M-V)$ matrix with null elements. The gradient and Hessian of function $\varphi_4(\mathbf{p})$ (eq. 25) are given by:

$$\boldsymbol{\nabla}\varphi_4(\mathbf{p}) = 2\mathbf{R}_4^\intercal \left(\mathbf{R}_4\mathbf{p} - \mathbf{a} \right) \quad , \tag{28}$$

and

$$\mathbf{H}_4(\mathbf{p}) = 2\mathbf{R}_4^{\mathsf{T}}\mathbf{R}_4 \quad . \tag{29}$$

The *source's horizontal location constraint* imposes that the horizontal Cartesian coordinates of the origin within the shallowest prism must be as close as possible to a known outcropping point given by the horizontal Cartesian coordinates $(\tilde{x}_0^0,\ \tilde{y}_0^0)$. This constraint is given by

$$\begin{aligned} \varphi_5(\mathbf{p}) &= \left[\left(x_0^1 - \tilde{x}_0^0\right)^2 + \left(y_0^1 - \tilde{y}_0^0\right)^2\right] \\ &= \left(\mathbf{R}_5\mathbf{p} - \mathbf{b}\right)^{\mathsf{T}}\left(\mathbf{R}_5\mathbf{p} - \mathbf{b}\right) \end{aligned} \quad , \tag{30}$$

where $\mathbf{b}$ is a 2×1 vector containing the horizontal Cartesian coordinates of the outcropping point

$$\mathbf{b} = \begin{bmatrix} \tilde{x}_0^0 & \tilde{y}_0^0 \end{bmatrix}^{\mathsf{T}} , \tag{31}$$

and

$$\mathbf{R}_5 = \begin{bmatrix} \mathbf{0}_{2\times V} & \mathbf{I}_2 & \mathbf{0}_{2\times(M-V-2)} \end{bmatrix}_{2\times M} , \tag{32}$$

where $\mathbf{0}_{2\times(M-V-2)}$ is a $2 \times (M - V - 2)$ matrix with null elements. The gradient and Hessian of function $\varphi_5(\mathbf{p})$ (eq. 30) are given by:

$$\boldsymbol{\nabla}\varphi_5(\mathbf{p}) = 2\mathbf{R}_5^{\mathsf{T}}\left(\mathbf{R}_5\mathbf{p} - \mathbf{b}\right) \quad , \tag{33}$$

and

$$\mathbf{H}_5(\mathbf{p}) = 2\mathbf{R}_5^{\mathsf{T}}\mathbf{R}_5 \quad . \tag{34}$$

2.3.3 Minimum Euclidean norm constraints

Two constraints use the zeroth-order Tikhonov regularization with the purpose of obtaining stable solutions without introducing prior information about the shape of the source. However, these two constraints combined with the interpretation model impose source compactness.

The *Minimum Euclidean norm of the radii* imposes that all estimated radii within each prism must be close to null values. This constraint was proposed by Oliveira Jr. et al. (2011) and Oliveira Jr. & Barbosa (2013) and can be rewritten as follows

$$\begin{aligned} \varphi_6(\mathbf{p}) &= \sum_{k=1}^{L}\sum_{j=1}^{V}\left(r_j^k\right)^2 \\ &= \mathbf{p}^{\mathsf{T}}\mathbf{R}_6^{\mathsf{T}}\mathbf{R}_6\mathbf{p} \end{aligned} \quad , \tag{35}$$

where

$$\mathbf{R}_6 = \begin{bmatrix} \mathbf{S}_6 & \mathbf{0}_{(M-1)\times 1} \\ \mathbf{0}_{1\times(M-1)} & 0 \end{bmatrix}_{M\times M} \quad , \tag{36}$$

and

$$\mathbf{S}_6 = \mathbf{I}_L \otimes \begin{bmatrix} \mathbf{I}_V & \mathbf{0}_{V\times 2} \\ \mathbf{0}_{2\times V} & \mathbf{0}_{2\times 2} \end{bmatrix}_{(V+2)\times(V+2)} \quad , \tag{37}$$

where $\mathbf{0}_{2\times 2}$ is a 2×2 matrix with null elements, $\mathbf{0}_{V\times 2}$ is a $V \times 2$ matrix with null elements and $\mathbf{0}_{2\times V}$ is a $2 \times V$ matrix with null elements. The gradient and Hessian of function $\varphi_6(\mathbf{p})$ (eq. 35) are given by:

$$\boldsymbol{\nabla}\varphi_6(\mathbf{p}) = 2\mathbf{R}_6^{\mathsf{T}}\mathbf{R}_6\mathbf{p} \quad , \tag{38}$$

and

$$\mathbf{H}_6(\mathbf{p}) = 2\mathbf{R}_6^{\mathsf{T}}\mathbf{R}_6 \quad . \tag{39}$$

The other constraint, the *Minimum Euclidean norm of the prism thickness*, imposes that the thickness of all prisms must be close to zero. We present this constraint to introduce a priori information about the maximum depth extent of the source which in turn is dependent on the depth to the top of the shallowest prism z_0. It is given by

$$\begin{aligned} \varphi_7(\mathbf{p}) &= dz^2 \\ &= \mathbf{p}^{\mathsf{T}}\mathbf{R}_7^{\mathsf{T}}\mathbf{R}_7\mathbf{p} \end{aligned} \quad , \tag{40}$$

where

$$\mathbf{R}_7 = \begin{bmatrix} \mathbf{0}_{(M-1)\times(M-1)} & \mathbf{0}_{(M-1)\times 1} \\ \mathbf{0}_{1\times(M-1)} & 1 \end{bmatrix}_{M\times M} \quad . \tag{41}$$

The gradient and Hessian of function $\varphi_7(\mathbf{p})$ (eq. 40) are given by:

$$\boldsymbol{\nabla}\varphi_7(\mathbf{p}) = 2\mathbf{R}_7^{\mathsf{T}}\mathbf{R}_7\mathbf{p} \quad , \tag{42}$$

and

$$\mathbf{H}_7(\mathbf{p}) = 2\mathbf{R}_7^{\mathsf{T}}\mathbf{R}_7 \quad . \tag{43}$$

2.4 Computational procedures

The computational procedures of our method require ....

2.4.1 Initial guess and inequality constraints

Estimating, from the total-field anomaly, the parameter vector $\mathbf{p}$ (eq. 1) that minimizes the goal function $\Gamma(\mathbf{p})$ (eq. 4) for a given pair of total-magnetization intensity m_0 and depth to the top of the shallowest prism z_0, subject to the inequality constraint (eq. 5) is a nonlinear inverse problem which requires an initial guess.

The initial guess of the 3D source shape is a simple cylinder with radius and horizontal Cartesian coordinates of its center were taken after computing the reduction-to-the-pole of the observed total-field anomaly (RTP anomaly). We start by computing the RTP anomaly, which in turn has three purposes. The first one is verify if the used total-magnetization direction is valid. The second purpose is define the upper and lower limits of the inequality constraints (eq. 5). Finally, the third purpose of the RTP anomaly is define the radius and horizontal Cartesian coordinates of the center of the a cylindrical body used as an initial guess.

If the source has a uniform magnetization direction, the RTP anomaly is predominantly positive and decays to zero close to its horizontal boundaries Reis et al. (2020). In this case, the declination and inclination are close to the ones used to obtain the RTP anomaly. The upper and lower limits in the inequality constraints (eq. 5) depend on the parameter. If the parameters are the radii of the vertices of all prisms (r_j^k, $j = 1, \ldots, V$, $k = 1, \ldots, L$, the lower limit is close to zero and the upper limit is approximately defined by the radius of a circular area encompassing the region where the RTP anomaly has its maximum and decays to zero. If the parameters are the horizontal coordinates (x_0^k and y_0^k, $k = 1, \ldots, L$) of the origins O^k, $k = 1, \ldots, L$, the upper and lower limits are the uppermost and lowermost $x-$ and $y-$ coordinates of a circular area encompassing the region where the RTP anomaly has its maximum and decays to zero. If the parameters are the thickness dz of all stacked prisms, we set a large value (e.g., 1 km) to the upper limit and a value close to zero to the lower limit .

The radius and the horizontal Cartesian coordinates of the center of the cylinder-like initial guess are defined, respectively, by the radius and the $x-$ and $y-$ coordinates of the center of a circular area encompassing the region where the RTP anomaly has its maximum and decays to its maximum gradient. This definition does not require a high accuracy. After defining by the RTP anomaly the radius and the horizontal Cartesian coordinates of the center of the cylinder-like initial guess, we set a guess to the thickness of this cylinder to generate a bottom depth greater than that we expect for the true source. Next, we run a forward modelling of the total-field anomaly aiming at adjusting the cylinder volume of the initial guess and finding the ranges of the total-magnetization intensity m_0 and to the depth to the top of source z_0 which yield a preliminary fit of the observed data.

Note that, this first step, to adjust the initial guess and to set the range of m_0 and z_0, is carried out before performing the inversion. In this step, we just perform a magnetic forward modelling by using the observed total-field anomaly only. Hence, no inversion is required.

2.4.2 Optimization algorithm

Here, we use the Levenberg-Marquardt algorithm (e.g., Aster et al. 2019, p. 240) to solve the non-linear inverse problem given by eqs. 4 and 5. The Levenberg-Marquardt algorithm is an iterative gradient-based method that, at each iteration κ, updates the estimate parameter vector $\hat{\mathbf{p}}_{(\kappa)}$ (where the superscript hat "ˆ" denotes estimated) to obtain a new estimated parameter vector $\hat{\mathbf{p}}_{(\kappa+1)}$. We compute this update by following the same strategy of Barbosa et al. (1999b), Oliveira Jr. et al. (2011) and Oliveira Jr. & Barbosa (2013) to incorporate the inequality constraint (eq. 5). This strategy consists in transforming each element $\hat{p}_l$ of the estimated parameter vector $\hat{\mathbf{p}}_{(\kappa)} \equiv \hat{p}_l \in (p_l^{min}, p_l^{max})$ into the element $\hat{p}_l^\dagger$ of a new vector $\hat{\mathbf{p}}_{(\kappa)}^\dagger \equiv \hat{p}_l^\dagger \in (-\infty, +\infty)$ as follows:

$$\hat{p}_l^\dagger = -\ln\left(\frac{p_l^{max} - \hat{p}_l}{\hat{p}_l - p_l^{min}}\right) , \tag{44}$$

where p_l^{min} and p_l^{max} are defined in the inequality constraint (eq. 5). Then, we compute a correction $\boldsymbol{\Delta}\hat{\mathbf{p}}_{(k)}^\dagger$ and a new vector $\hat{\mathbf{p}}_{(\kappa+1)}^\dagger = \hat{\mathbf{p}}_{(\kappa)}^\dagger + \boldsymbol{\Delta}\hat{\mathbf{p}}_{(\kappa)}^\dagger$. Finally, we transform each element $\hat{p}_l^\dagger$ of $\hat{\mathbf{p}}_{(\kappa+1)}^\dagger$ into the element $\hat{p}_l$ of the new estimated parameter vector $\hat{\mathbf{p}}_{(\kappa+1)}$ as follows:

$$\hat{p}_l = p_l^{min} + \left(\frac{p_l^{max} - p_l^{min}}{1 + e^{-\hat{p}_l^\dagger}}\right) . \tag{45}$$

2.4.3 Choice of weights $\alpha_1 - \alpha_7$

Attributing values to the weights α_ℓ (eq. 4) is an important feature of our method. However, there is no analytical rule to define them and their values can be dependent on the particular characteristics of the type of geological setting where the method is being applied Silva et al. (2001). To overcome this problem, we normalize the α_ℓ values as follows:

$$\alpha_\ell = \tilde{\alpha}_\ell \frac{E_\phi}{E_\ell}, \quad \ell = 1, \ldots, 7, \tag{46}$$

where $\tilde{\alpha}_\ell$ is a positive scalar and E_ϕ/E_ℓ is a normalizing factor allowing the $\tilde{\alpha}_\ell$ to be independent of the physical units used. In this equation, E_ℓ represents the trace of the Hessian matrix $\mathbf{H}_\ell$ (eqs 14, 19, 24, 29, 34, 39, and 43) of the ℓth constraining function $\varphi_\ell(\mathbf{p})$ (eqs 11, 15, 20, 25, 30, 35, and 40). The constant E_ϕ is the trace of the Hessian matrix $\mathbf{H}_\phi(\mathbf{p}_0)$ (eq. 10) of the misfit function $\phi(\mathbf{p})$ (eq. 6) computed with the initial approximation $\hat{\mathbf{p}}_{(0)}$ for the parameter vector $\mathbf{p}$ (eq. 1) at the beginning of the inversion algorithm. According to this empirical strategy, the weights α_ℓ are defined using the positive scalars $\tilde{\alpha}_\ell$ (eq. 46), which are less dependent on the particular characteristics of the interpretation geological setting.

2.4.4 Inversion algorithm

At each iteration κ of our algorithm for minimizing the goal function $\Gamma(\mathbf{p})$ (eq. 4), the correction $\boldsymbol{\Delta}\hat{\mathbf{p}}_{(\kappa)}^\dagger$ is computed by solving the following linear system through XXXXXXX:

$$\mathbf{Q}_{(\kappa)}^{-1}\left[\mathbf{Q}_{(k)}\mathbf{H}^\dagger(\hat{\mathbf{p}}_{(\kappa)})\mathbf{Q}_{(\kappa)} + \lambda_{(\kappa)}\mathbf{I}_M\right]\mathbf{Q}_{(\kappa)}^{-1}\boldsymbol{\Delta}\hat{\mathbf{p}}_{(\kappa)}^\dagger = -\boldsymbol{\nabla}\Gamma(\hat{\mathbf{p}}_{(\kappa)}) , \tag{47}$$

where $\lambda_{(\kappa)}$ is a positive scalar (known as Marquardt parameter) which is adjusted at each iteration and is associated with the Levenberg-Marquardt method (e.g., Silva et al. 2001; Aster et al. 2019, p. 240), $\mathbf{I}_M$ is the identity matrix with order M, $\boldsymbol{\nabla}\Gamma(\hat{\mathbf{p}}_{(\kappa)})$ is the gradient of the goal function (eq. 7) and $\mathbf{H}^{\dagger}(\hat{\mathbf{p}}_{(\kappa)})$ is a matrix given by

$$\mathbf{H}^{\dagger}(\hat{\mathbf{p}}_{(\kappa)}) = \mathbf{H}(\hat{\mathbf{p}}_{(\kappa)})\mathbf{T}(\hat{\mathbf{p}}_{(\kappa)}), \tag{48}$$

where $\mathbf{H}(\hat{\mathbf{p}}_{(\kappa)})$ is the Hessian matrix of the goal function (eq. 8) and $\mathbf{T}(\hat{\mathbf{p}}_{(\kappa)})$ is a diagonal matrix whose element ll is given by

$$t(\hat{p}_l) = \frac{(p_l^{max} - \hat{p}_l)(\hat{p}_l - p_l^{min})}{p_l^{max} - p_l^{min}}, \quad l = 1, \ldots, M\ , \tag{49}$$

with p_l being the lth element of the estimated parameter vector $\hat{\mathbf{p}}_{(\kappa)}$. To prevent null values from occurring in any diagonal element of $\mathbf{T}(\hat{\mathbf{p}}_{(\kappa)})$ (eq. 48), we follow Barbosa et al. (1999b) who added a small positive number (on the order of 10^{-2}) to each term of the numerator in eq. 49. In eq. 47, $\mathbf{Q}_{(\kappa)}$ is a diagonal matrix proposed by Marquardt (1963) for scaling the parameter $\lambda_{(\kappa)}$ at each iteration and improving the convergence of the algorithm. The element ll of this diagonal matrix $\mathbf{Q}_{(\kappa)}$ is given by

$$q_{ll} = \frac{1}{\sqrt{h_{ll}^{\dagger}}}\ , \tag{50}$$

where $h_{ll}^{\dagger}$ is the element ll of the matrix $\mathbf{H}^{\dagger}(\hat{\mathbf{p}}_{(\kappa)})$ (eq. 48).

After estimating $\boldsymbol{\Delta}\hat{\mathbf{p}}^{\dagger}_{(\kappa)}$ at the κth iteration by solving the linear system given in eq. 47, we update $\hat{\mathbf{p}}^{\dagger}_{(\kappa+1)}$, i.e.:

$$\hat{\mathbf{p}}^{\dagger}_{(\kappa+1)} = \hat{\mathbf{p}}^{\dagger}_{(\kappa)} + \boldsymbol{\Delta}\hat{\mathbf{p}}^{\dagger}_{(\kappa)}. \tag{51}$$

Next, we update the constrained parameter vector $\hat{\mathbf{p}}_{(\kappa+1)}$ by using eq. 45. Finaly, we stop the iterative process by evaluating the invariance of the goal function (eq. 4) along the iterations. Specifically, we check if the inequality

$$\left|\frac{\Gamma(\hat{\mathbf{p}}_{(\kappa+1)}) - \Gamma(\hat{\mathbf{p}}_{(\kappa)})}{\Gamma(\hat{\mathbf{p}}_{(\kappa)})}\right| \leq \tau \tag{52}$$

holds. In eq. 52, τ is a threshold value on the order of 10^{-3} to 10^{-4}.

2.4.5 Practical considerations

Our algorithm depends on several variables that significantly impact the estimated models and cannot be automatically set without the interpreter's judgment. They are the $\tilde{\alpha}_1 - \tilde{\alpha}_7$ (eq. 46). Based on our practical experience, we suggest some empirical procedures for setting these parameters.

The parameters $\tilde{\alpha}_1$ and $\tilde{\alpha}_2$ impose prior information on the shape of the horizontal cross-section of the prisms. The first one forces all prisms to have a circular horizontal cross-section, while the second forces all prisms to have a similar horizontal cross-section. Generally, their values vary from 10^{-5} to 10^{-3} and differs from each other by one order of magnitude, at most. The parameter $\tilde{\alpha}_3$ also varies from 10^{-5} to 10^{-3} and controls the relative position of adjacent prisms forming the model. A high value privileges a vertical estimated body, whereas a small value tends to generate an inclined estimated body.

In comparison to $\tilde{\alpha}_1$, $\tilde{\alpha}_2$ and $\tilde{\alpha}_3$, the other parameters usually have smaller values varying from 10^{-8} to 10^{-4}. The parameters $\tilde{\alpha}_4$ and $\tilde{\alpha}_5$ are used when a priori information about the source is available at the study area. The parameter $\tilde{\alpha}_6$ has a purely mathematical meaning and it is used only to obtain stable solutions for the inverse problem. Its value is set to be as small as possible. The parameter $\tilde{\alpha}_7$ controls the total-vertical extension of the the estimated body. The greater its value, the shallower the estimated depth to the bottom of the source will be and vice versa. A general rule is starting with values $\tilde{\alpha}_1 = 10^{-4}$, $\tilde{\alpha}_2 = 10^{-4}$, $\tilde{\alpha}_3 = 10^{-4}$, $\tilde{\alpha}_4 = 0$, $\tilde{\alpha}_5 = 0$, $\tilde{\alpha}_6 = 10^{-7}$, $\tilde{\alpha}_7 = 10^{-5}$ and change them to refine the results.

3 APPLICATION TO SYNTHETIC DATA

3.1 Simple model test

We have simulated a lopolithic intrusion, a funnel-shaped source (Cawthorn & Miller 2018), with simple geometry (blue prisms in Figs 3b and 4), which extends from $z_0 = 0$ m to $1,600$ m along depth and satisfies most of the constraints described in subsection 2.3. It is formed by $L = 8$ prisms, all of them with the same number of vertices $V = 20$, thickness $dz = 200$ m and horizontal coordinates $(x_0^k, y_0^k) = (0, 0)$ m of the origins O^k, $k = 1, \ldots, L$. The radii of all vertices are equal to each other within the same prism and decrease linearly with depth, varying from $r_j^0 = 1\,920$ m, at the shallowest prism, $r_j^L = 800$ m, at the deepest prism, $j = 1, \ldots, V$. All prisms have the same total-magnetization direction with inclination $-50°$, declination $9°$ and intensity $m_0 = 9$ A/m. We calculated the total-field anomaly produced by this simple model, in an area of 100 km^2 area, by simulating an airborne survey composed of 21 flight lines that are equally spaced 500 m apart along the y axis, at a constant vertical coordinate $z = -150$ m. At each line, there are 101 observation points spaced 100 m apart along x axis. The main geomagnetic field direction simulated was $-21.5°$ and $-18.7°$ for the inclination and declination, respectively. The total-field anomaly is corrupted with a pseudorandom Gaussian noise having mean $\mu_0 = 0$ nT and and standard deviation $\sigma_0 = 5$ nT (Fig. 3a).

We have inverted the noise-corrupted total-field anomaly (Fig. 3a) produced by the simulated lopolith-like body (blue prisms in Fig. 3b) and obtained 36 different estimates. Each estimate was obtained by using six different pairs of depth to the top z_0 and total-magnetization intensity m_0. The ranges of z_0 and m_0 are shown in Fig. 3c. Fig. 3d shows the RTP anomaly obtained from the noise-corrupted total-field anomaly (Fig. 3a). Note that the RTP anomaly exhibits predominantly positive values and decays to zero. As previously mentioned, the RTP anomaly is used to set up the initial guess. The blue circle in Fig. 3d represents the horizontal projection of the initial approximation $\hat{\mathbf{p}}_{(0)}$ whose shape is a vertical cylinder. All estimates were generated by using the true values of total-magnetization inclination and declination, the same interpretation model formed by $L = 5$ prisms, each one with $V = 20$ vertices, and the same weights for the constraining functions: $\tilde{\alpha}_1 = 10^{-5}$, $\tilde{\alpha}_2 = 10^{-4}$, $\tilde{\alpha}_3 = 10^{-4}$, $\tilde{\alpha}_4 = 0$, $\tilde{\alpha}_5 = 0$, $\tilde{\alpha}_6 = 10^{-7}$, and $\tilde{\alpha}_7 = 10^{-6}$. In all inversions, the initial approximation $\hat{\mathbf{p}}_{(0)}$ (red prisms in Fig. 4b) has the same constant radii $r_j^k = 2,000$ m, $k = 1, \ldots, L$, $j = 1, \ldots, V$, the same prism thicknesses $dz = 350$ m and the same origins $(x_0^k, y_0^k) = (0, 0)$ m for all prisms.

Fig. 3c shows the discrete mapping of the goal functional $\Gamma(\mathbf{p})$ (eq. 4) on the plane of the total-magnetization intensity (m_0) versus depth to the top (z_0). The true values of depth to the top z_0 and total-magnetization intensity m_0 (represented by the red triangle in Fig. 3c) produces the smallest value of goal function $\Gamma(\mathbf{p})$ (eq. 4) that will be taken as the best estimated model. This estimated model (red prisms in Figs 4c and d) not only fits the noise-corrupted data (Fig. 4a), but also retrieves the geometry of the true model (blue prisms in Figs 4b-d). The inset in Fig. 4a shows that the residuals follow a normal distribution with mean μ and standard deviation σ compatible with those values used to generate the synthetic noise. The estimated thickness of each prism is $dz = 298.13$ m resulting in a depth-to-bottom estimate ($1,490.65$ m) very close to the true one ($1,600$ m). These results illustrate the good performance of our method in an ideal case.

3.2 Dipping model test

Fig. 5a shows the noise-corrupted total-field anomaly produced by an outcropping low-angle dipping volcanic duct (blue prisms in Figs 5c and d) embedded in nonmagnetic host rocks. The simulated magnetic data are contaminated with a pseudorandom Gaussian noise having mean of $\mu_0 = 0$ nT and standard deviation of $\sigma_0 = 5$ nT. We simulated airborne magnetic survey whose flight heights ranging from 0 to 720 m (Fig. 5b) and resulting in a total of 1,694 measurements. The simulated dipping source has total-magnetization direction with inclination $-50°$, declination $9°$ and intensity $m_0 = 9$ A/m. The main geomagnetic field direction has inclination of $-21.5°$ and declination of $-18.7°$. To set up the simulated dipping source (blue prisms in Figs 5c and d), we used $L = 8$ prisms, all of them with the same number of vertices $V = 20$ and thickness $dz = 380$ m. The horizontal coordinates of the center of the shallowest prism that composes the simulated dipping source are $(x_0^1, y_0^1) = (-300, 600)$ m. The simulated dipping source has a top 0 m deep ($z_0 = 0$) and a base 3,040 m deep.

To set up the initial guess and other variables in the inversion, we calculate the RTP anomaly (Fig. 6a) of the noise-corrupted total-field anomaly (Fig. 5a). Fig. 6b shows the goal function (eq. 4) on the plane $z_0 \times m_0$ produced by 36 estimates obtained with a grid of 6×6 tentative values of depth to the top z_0 and total-magnetization intensity m_0.

All 36 estimates were generated by using the true values of total-magnetization inclination and declination, the same interpretation model formed by $L = 5$ prisms, each one with $V = 20$ vertices, and the same weights for the constraining functions: $\tilde{\alpha}_1 = 10^{-3}$, $\tilde{\alpha}_2 = 10^{-3}$, $\tilde{\alpha}_3 = 10^{-6}$, $\tilde{\alpha}_4 = 0$, $\tilde{\alpha}_5 = 0$, $\tilde{\alpha}_6 = 10^{-3}$, and $\tilde{\alpha}_7 = 10^{-5}$.

The optimum solution is the one that produces the smallest value of the discrete mapping of the goal function (Fig. 6b). The white diamond in Fig. 6b pinpoints the minimum of the goal function which is achieved when the estimated body has a top 20 m deep and a total-magnetization intensity of 12 A/m. Note that the depth to the top of estimated body is deeper than the true one; however, the total-magnetization intensity was retrieved correctly.

Fig. 7a shows the magnetic-data residuals, defined as the difference between the synthetic noise-corrupted magnetic data in Fig. 5a and the predicted data (not shown). Fig. 7a shows the simulated dipping source (blue prisms) and the cylinder-like initial guess (red prisms) with thickness $dz = 350$ m and and the same origins $(x_0^k, y_0^k) = (-200, 0)$ m for all prisms. Note that the estimated source (red prisms in Figs.7c and d) with $z_0 = 20$ m and $m_0 = 12$ A/m (pinpointed as the white diamond in Fig. 6b) retrieved the shape of the simulated dipping source (blue prisms) reasonably, although the retrieved depth to the bottom of 3,453.0 m was deeper than the true one. The retrieved deep-bottomed dipping source is because that the depth to the top of estimated body has been deeper than the true one.

3.3 Complex model test

We have simulated a complex inclined body (blue prisms in Figs 8 and 9) inspired by an alkaline vertical dipping intrusion. The simulated intrusion extends from $z_0 = 130$ m to 5270 m along depth and violates most of the constraints described in subsection 2.3. It is formed by $L = 10$ prisms, all of them with the same number of vertices $V = 30$ of thickness $dz = 600$ m. The horizontal coordinates of the origins O^k vary linearly from $(x_0^0, y_0^0) = (-250, 750)$ m, at the shallowest prism, to $(x_L^0, y_L^0) = (250, -750)$ m resulting a dip in the direction NW-SE, at the deepest prism. The displacements of the horizontal coordinates of the origins O_k resulted in a simulated source dipping to northwest (blue prisms in Figs 8 and 9). The radii $r_j^k, k = 1, \ldots, L, j = 1, \ldots, V$, defining the vertices vary from 240 m to 1 540 m and also differ from each other within the same prism. All prisms have a constant total magnetization with inclination $-50°$, declination $9°$ and intensity $m_0 = 12$ A/m. We are simulating an alkaline vertical dipping intrusion. We have calculated the total-field anomaly produced by this complex model, in an area of 100 km^2, by simulating an airborne survey composed of 18 north-south flight lines distributed from $-5\,000$ m to $5\,000$ m along the y axis and a single east-west tie line approximately located at $x = 0$ m. The data points are located on the undulated surface shown in Fig. 8a. Notice that both flight and tie lines are not perfectly straight. To compute the synthetic total-field anomaly, we consider a constant main field with inclination $-21.5°$ and declination $-18.7°$, which is significantly different from the total-magnetization direction of the complex model. Finally, we have contaminated the synthetic total-field anomaly with a pseudorandom Gaussian noise having mean and standard deviation equal to 0 nT and 5 nT, respectively (Fig. 8a).

We have inverted the noise-corrupted total-field anomaly (Fig. 8a) produced by the complex model by using 36 different pairs of depth to the top z_0 and total-magnetization intensity m_0 (Fig. **??**). Differently from the previous simulation with a simple model, the present generated grid of m_0 and z_0 does not contain the true ones (represented by the red triangle in Fig. **??**). All models were generated by using the true direction of the main geomagnetic field (i.e., inclination $-21.5°$ and declination

$-18.7°$), the same interpretation model formed by $L = 8$ prisms, each one with $V = 20$ vertices, and the same weights for the constraining functions: $\tilde{\alpha}_1 = 10^{-5}$, $\tilde{\alpha}_2 = 10^{-4}$, $\tilde{\alpha}_3 = 10^{-4}$, $\tilde{\alpha}_4 = 0$, $\tilde{\alpha}_5 = 0$, $\tilde{\alpha}_6 = 10^{-7}$, and $\tilde{\alpha}_7 = 10^{-5}$. The initial approximation $\hat{\mathbf{p}}_{(0)}$ for all inversions (red prisms in Fig. 8b) has the same constant radii $r_j^k = 800$ m, $k = 1, \ldots, L$, $j = 1, \ldots, V$, the same thickness $dz = 650$ m and the same origin $(x_0^k, y_0^k) = (-300, 300)$ m for all prisms.

Fig. **??** shows the goal function $\Gamma(\mathbf{p})$ (eq. 4), with different total-magnetization intensity m_0 and depth-to-the-top z_0 on the plane ($m_0 \times z_0$). We note that a minimum region (dark blue region in Fig. **??**) contains the true pair of m_0 and z_0 (red triangle in Fig 7). However, we do not use the true m_0 and z_0 to retrieve the magnetized source because, intentionally in this test, our coarse mapping of the goal function $\Gamma(\mathbf{p})$ does not include them. Nevertheless, a well-defined minimum of the goal function value (pinpointed as the white diamond in Fig. **??**) is achieved when the total-magnetization intensity $m_0 = 12.6$ A/m and depth to the top at $z_0 = 150$ m. These values of m_0 and z_0 will be used to retrieve the estimated model.

Fig. 9 shows the estimated model (red prisms in Figs 9c and d) obtained by using the values of m_0 and z_0 represented by the white diamond in Fig. **??**. Note that the this estimated model fits the noise-corrupted data and also retrieves the geometry of the true source (blue prisms). The inset in Fig. 9a shows that the residuals follow a normal distribution with mean μ and standard deviation σ compatible with those values used to generate the noise-corrupted data. The estimated of depth to the bottom (5 662.2 m) and volume (11.56 km^3) are underestimated, but still close to the true values (5 570 m and 12.60 km^3). These results show that our method can also be very useful to interpret complex sources, even if they do not perfectly satisfy the constraints imposed to solve the nonlinear inverse problem.

4 APPLICATION TO FIELD DATA

We have applied our method to interpret airborne magnetic data provided by Geological Survey of Brazil (CPRM) over the Anitápolis complex, in southern Brazil. The airborne survey was flown with north-south and east-west lines spaced by 500 m and $10\,000$ m from each other, respectively. The total-field anomaly data were corrected from daytime variation and from the main geomagnetic field using the IGRF. The inclination, declination and intensity of the main geomanetic field at the study area, for the period of the survey, are $-37.05°$, $-18.17°$ and $\approx 22\,768$ nT, respectively. The residual total-field anomaly shown in Fig. 10a was obtained by removing a second-order polynomial from the original data (not shown). Figs 10b and 10c show the geometric height the observed data and the topography of the study area, respectively. For convenience, we have subtracted 800 m from their values.

The Anitápolis alkaline-carbonatitic complex forms a circular concentric body (≈ 6 km^2 in area) containing magnetite as part of its mineralogical composition. It intruded into the Late Proterozoic leucogranites of the Dom Feliciano mobile belt in the Early Cretaceous (132 Ma), apparently concomitant with the voluminous flood tholeiitic basalts of the Serra Geral Formation (133-130 Ma) at the southern side of the Paraná Basin (Gibson et al. 1999; Scheibe et al. 2005). As pointed out by Gomes et al. (2018), there is still some debate about the emplacement of the Anitápolis alkaline-carbonatitic complex. Melcher & Coutinho (1966) pointed out the influence of N-S-trending faults. Horbach & Marimon (1980) affirmed that the Anitápolis complex is controlled by a large N30W lineament. Scheibe et al. (2005) considered that it is roughly emplaced along the E-W Rio Uruguay Lineament. According to Riccomini et al. (2005), the Anitápolis complex does not show a clear structural control.

We set the total-magnetization direction of the interpretation model with inclination $I = -21°$ and declination $D = -11°$. These values were estimated by Reis et al. (2019) for the study area by using a method based on the equivalent-layer technique (Dampney 1969; Emilia 1973). We have verified this estimated direction using the reduction to the pole technique (not shown). This total-magnetization direction indicates the presence of remanent magnetization. Laboratory measurements on rock samples obtained at the Jacupiranga complex, another alkaline complex located northward of the study area, with the same age as the Anitápolis complex, show total-magnetization intensities values varying from approximately 0.01 to 29.90 A/m (Alva-Valdivia et al. 2009, tb. 1). We used these values as a priori information to set the range of possible values for the total-magnetization intensity m_0 in the Anitápolis complex.

We used an interpretation model formed by $L = 6$ prisms, each one with $V = 20$ vertices defining their horizontal cross-sections. We inverted the observed total-field anomaly (Fig. 10a) for each pair of m_0 and z_0 shown in Fig. **??**, resulting in 100 estimated models. For all models, we set the same initial approximation $\hat{\mathbf{p}}_{(0)}$ (red prisms in Figs 11b and 12b) with origin at $(x_0^k, y_0^k) = (6921, 688)$

km, constant radii $r_j^k = 700$ m for all vertices forming all prisms and the same constant thickness $dz = 900$ m. We also set the same weights which were used in the synthetic tests, i.e., $\tilde{\alpha}_1 = 10^{-4}$, $\tilde{\alpha}_2 = 10^{-3}$, $\tilde{\alpha}_3 = 10^{-4}$, $\tilde{\alpha}_4 = 0$, $\tilde{\alpha}_5 = 0$, $\tilde{\alpha}_6 = 10^{-8}$, and $\tilde{\alpha}_7 = 10^{-5}$ (eq. 46).

Fig. **??** shows that there is a region containing candidate solutions producing small values of the goal function $\Gamma(\mathbf{p})$ (eq. 4), with different values of m_0 and z_0. The pink diamond in Fig. **??** represents the non-outcropping estimated model shown in Fig. 11. This model produces not only the smallest value for $\Gamma(\mathbf{p})$ (eq. 4), but also reasonable data fit (Fig. 11a). It has a volume 9.96 km^3, total thickness of $4\,596.55$ m ($dz = 766.10$), depth-to-the-top $z_0 = 20$ m and total-magnetization intensity $m_0 = 14.0$ A/m. The non-outcropping estimated model (Figs 11c and d) is compatible with a priori information because we do not have evidences of an outcropping source for this anomaly, although there are outcropping intrusions in the area of the Anitápolis complex (Gibson et al. 1999). Besides, its total-magnetization intensity $m_0 = 14$ A/m is within the range found by Alva-Valdivia et al. (2009) for intrusions located at the Jacupiranga complex.

The white diamond in Fig. **??** represents the alternative model show in Fig. 12. This model is similar to that shown in Fig. 11. It has a volume 9.57 km^3, total thickness $4\,419.34$ m ($dz = 736.56$), depth-to-the-top $z_0 = 0$ m and total-magnetization intensity $m_0 = 14$ A/m. In comparison with the non-outcropping model shown in Fig. 11, the alternative model shown in Fig. 12 has very similar geometry, but it outcrops. Both estimated models show a nearly N30W elongated body with accentuated dip along depth (Figs 11 and 12), which coincides with the topographic low observed in Fig 10c. Hence, these estimates agree with the interpretation proposed by Horbach & Marimon (1980), that considered the presence of N30W-trending fault controlling the Anitápolis complex.

5 CONCLUSIONS

We have developed a total-field anomaly nonlinear inversion to estimate the shape of an isolated 3-D geological body assuming the knowledge about its total-magnetization direction. We approximate the body by a set of vertically stacked right prisms. The horizontal cross-section of each prism is a polygon defined by a given number of equally spaced vertices from 0° to 360°. We peformed our inversion for a set of given depths to the top and total-magnetization intensities these results illustrate the inherent ambiguity of potential-field methods in retrieving both the physical-property distribution and volume of the sources. In this case, some a priori information must be used to constraint the range of reliable solutions. For each depth to the top and total-magnetization intensity, our method estimates the geometries of the cross-sections (the radii associated with the polygon vertices), the thickness and the horizontal positions of the prisms. The estimated model approximates the 3-D geological body by solving a constrained nonlinear magnetic inversion. The estimated bodies producing the smallest values of the goal function form the set of candidate solutions that yields an acceptable data fitting satisfying the constraints on the source shape. Our method is an extension of previous works developed for retrieving the geometry of 3-D bodies by inverting gravity and gravity-gradient data. We not only adapted the previous methods for interpreting total-field anomaly data, but also generalized them to include the depth to the top and depth extension of the prisms among the estimated parameters.

Results obtained with synthetic data produced by a simple symmetric source and by a realistic geological source, with variable dip and shape along depth, show that our method is able to retrieve the source's shape and fit the data in both cases. We applied our method to interpret a total-field anomaly data over the alkaline-carbonatitic complex of Anitápolis, in southern Brazil. We obtained two candidate models having similar shapes, depths to the top and total-magnetic intensities, all of them consistent with the available geological information. Both estimated models suggest that the emplacement of the Anitápolis complex seems to be controlled by a nearly N30W-trending fault in agreement with previous studies. It is important to bear in mind, however, the possible bias in the geometry of the estimated body due to errors in the total-magnetization direction used as a priori information. Possible extensions of this work is the inversion of elongated and/or multiple sources. In addition, an the combination of gradient-based and heuristic optimization methods could be applied to estimate optimal regularization weights, overcoming problems with local minima.

ACKNOWLEDGMENTS

We thank the Brazilian geological service CPRM for providing the field data. Leonardo Vital thanks the PhD. scholarship from CAPES (Finance Code 001). Vanderlei Oliveira Jr. thanks the fellowships from CNPQ (grant 308945/2017-4) and FAPERJ (grant E-26/202.729/2018). Valeria Barbosa thanks the fellowships from CNPQ (grant 307135 /2014-4) and FAPERJ (grant 26/202.582/2019).

REFERENCES

Abedi, M., Asghari, O., & Norouzi, G.-H., 2015. Collocated cokriging of iron deposit based on a model of magnetic susceptibility: a case study in Morvarid mine, Iran, *Arabian Journal of Geosciences*, **8**(4), 2179–2189.

Alva-Valdivia, L. M., Perrin, M., Rivas-Sánchez, M. L., Goguitchaichvili, A., López-Loera, H., Lopes, O. F., & Bonás, T. B., 2009. Rock magnetism and microscopy of the jacupiranga alkaline-carbonatitic complex, southern brazil, *Earth, Planets and Space*, **61**(1), 161–171.

Aster, R. C., Borchers, B., & Thurber, C. H., 2019. *Parameter Estimation and Inverse Problems*, Elsevier, 3rd edn.

Ballantyne, E. J., 1980. Magnetic curve fit for a thin dike; calculator program (TI 59), *Geophysics*, **45**(3), 447–455.

Barbosa, V. C. & Silva, J. B., 2006. Interactive 2d magnetic inversion: A tool for aiding forward modeling and testing geologic hypotheses, *Geophysics*, **71**(5), L43–L50.

Barbosa, V. C. F., Silva, J. B. C., & Medeiros, W. E., 1997. Gravity inversion of basement relief using approximate equality constraints on depths, *Geophysics*, **62**, 1745–1757.

Barbosa, V. C. F., Silva, J. B. C., & Medeiros, W. E., 1999a. Gravity inversion of a discontinuous relief stabilized by weighted smoothness constraints on depth, *Geophysics*, **64**(5), 1429–1437.

Barbosa, V. C. F., Silva, J. B. C., & Medeiros, W. E., 1999b. Stable inversion of gravity anomalies of sedimentary basins with nonsmooth basement reliefs and arbitrary density contrast variations, *Geophysics*, **64**(3), 754–764.

Bhattacharyya, B. K., 1980. A generalized multibody model for inversion of magnetic anomalies, *Geophysics*, **45**(2), 255–270.

Caratori Tontini, F., Cocchi, L., & Carmisciano, C., 2006. Depth-to-the-bottom optimization for magnetic data inversion: Magnetic structure of the latium volcanic region, italy, *Journal of Geophysical Research*, **111**, B11104.

Cawthorn, R. & Miller, J., 2018. Lopolith – A 100 year-old term. Is it still definitive?, *South African Journal of Geology*, **121**(3), 253–260.

Cella, F. & Fedi, M., 2012. Inversion of potential field data using the structural index as weighting function rate decay: Inversion of potential field data, *Geophysical Prospecting*, **60**(2), 313–336.

Cribb, J., 1976. Application Of The Generalized Linear Inverse To The Inversion Of Static Potential Data, *Geophysics*, **41**(6), 1365–1369.

Dampney, C. N. G., 1969. The equivalent source technique, *Geophysics*, **34**(1), 39–53.

Emilia, D. A., 1973. Equivalent sources used as an analytic base for processing total magnetic field profiles, *Geophysics*, **38**(2), 339–348.

Gibson, S. A., Thompson, R. N., Leonardos, O. H., Dickin, A. P., & Mitchell, J. G., 1999. The limited extent of plume-lithosphere interactions during continental flood-basalt genesis: geochemical evidence from cretaceous magmatism in southern Brazil, *Contributions to Mineralogy and Petrology*, **137**(1), 147–169.

Golub, G. H. & Loan, C. F. V., 2013. *Matrix Computations (Johns Hopkins Studies in the Mathematical Sciences)*, Johns Hopkins University Press, 4th edn.

Gomes, C. d. B., Comin-Chiaramonti, P., Azzone, R. G., Ruberti, E., & Rojas, G. E. E., 2018. Cretaceous carbonatites of the southeastern Brazilian Platform: a review, *Brazilian Journal of Geology*, **48**, 317 – 345.

Hidalgo-Gato, M. C. & Barbosa, V. C. F., 2019. Fast 3d magnetic inversion of a surface relief in the space domain, *Geophysics*, **84**(5), J57–J67.

Horbach, R. & Marimon, R. G., 1980. *Esboço da evolução tectônica e seu significado na gênese dos depósitos de fluorita no sudeste catarinense*, vol. 3, pp. 1540–1551, Sociedade Brasileira de Geologia, Camboriú, SC, Brazil.

Horn, R. A. & Johnson, C. R., 1991. *Topics in Matrix Analysis*, Cambridge University Press, 1st edn.

Last, B. J. & Kubik, K., 1983. Compact gravity inversion, *GEOPHYSICS*, **48**(6), 713–721.

Li, W., Lu, W., Qian, J., & Li, Y., 2017. A multiple level-set method for 3d inversion of magnetic data, *Geophysics*, **82**(5), J61–J81.

Li, Y. & Oldenburg, D. W., 1996. 3-D inversion of magnetic data, *Geophysics*, **61**(2), 394–408.

Marquardt, D. W., 1963. An algorithm for least-squares estimation of nonlinear parameters, *Journal of the society for Industrial and Applied Mathematics*, **11**(2), 431–441.

Melcher, G. C. & Coutinho, J. M. V., 1966. Rochas alcalinas e carbonatito de Anitápolis, estado de Santa Catarina, *Boletim da Sociedade Brasileira de Geologia*, **15**(1), 59–93.

Oliveira Jr., V. C. & Barbosa, V. C. F., 2013. 3-D radial gravity gradient inversion, *Geophysical Journal International*, **195**(2), 883–902.

Oliveira Jr., V. C., Barbosa, V. C. F., & Silva, J. B. C., 2011. Source geometry estimation using the mass excess criterion to constrain 3-D radial inversion of gravity data, *Geophysical Journal International*, **187**(2), 754–772.

Pignatelli, A., Nicolosi, I., & Chiappini, M., 2006. An alternative 3d inversion method for magnetic anomalies with depth resolution, *Annals of geophysics = Annali di geofisica*.

Pilkington, M., 1997. 3-D magnetic imaging using conjugate gradients, *Geophysics*, **62**(4), 1132–1142.

Pilkington, M., 2009. 3d magnetic data-space inversion with sparseness constraints, *Geophysics*, **74**(1), L7–L15.

Plouff, D., 1976. Gravity and magnetic fields of polygonal prisms and application to magnetic terrain corrections, *Geophysics*, **41**(4), 727–741.

Portniaguine, O. & Zhdanov, M. S., 1999. Focusing geophysical inversion images, *Geophysics*, **64**(3), 874–887.

Portniaguine, O. & Zhdanov, M. S., 2002. 3-D magnetic inversion with data compression and image focusing, *Geophysics*, **67**(5), 1532–1541.

Reis, A. L. A., Oliveira Jr., V. C., & Barbosa, V. C. F., 2019. *Equivalent layer technique for estimating magnetization direction*, pp. 1769–1773.

Reis, A. L. A., Jr., V. C. O., & Barbosa, V. C. F., 2020. Generalized positivity constraint on magnetic equivalent layers, *GEOPHYSICS*, **85**(6), 1–12.

Riccomini, C., Velázquez, V., & Gomes, C., 2005. Tectonic controls of the Mesozoic and Cenozoic alkaline magmatism in the central-southeastern brazilian platform, in *Mesozoic to Cenozoic Alkaline Magmatism in the Brazilian Platform*, chap. 2, pp. 31–55, eds Comin-Chiaramonti, P. & Gomes, C., Edusp/Fapesp, São Paulo.

Scheibe, L., Furtado, S., Comin-Chiaramonti, P., & Gomes, C., 2005. Cretaceous alkaline magmatism from Santa Catarina state, southern brazil, in *Mesozoic to Cenozoic Alkaline Magmatism in the Brazilian Platform*, chap. 16, pp. 523–571, eds Comin-Chiaramonti, P. & Gomes, C., Edusp/Fapesp, São Paulo.

Shamsipour, P., Chouteau, M., & Marcotte, D., 2011. 3d stochastic inversion of magnetic data, *Journal of Applied Geophysics*, **73**(4), 336–347.

Silva, J. B. C. & Hohmann, G. W., 1983. Nonlinear magnetic inversion using a random search method, *Geophysics*, **48**(12), 1645–1658.

Silva, J. B. C., Medeiros, W. E., & Barbosa, V. C. F., 2001. Potential-field inversion: Choosing the appropriate technique to solve a geologic problem, *GEOPHYSICS*, **66**(2), 511–520.

Uieda, L., Oliveira Jr., V. C., & Barbosa, V. C. F., 2013. Modeling the earth with fatiando a terra, in *Proceedings of the 12th Python in Science Conference*, pp. 96 – 103.

Wang, X. & Hansen, R. O., 1990. Inversion for magnetic anomalies of arbitrary three-dimensional bodies, *Geophysics*, **55**(10), 1321–1326.

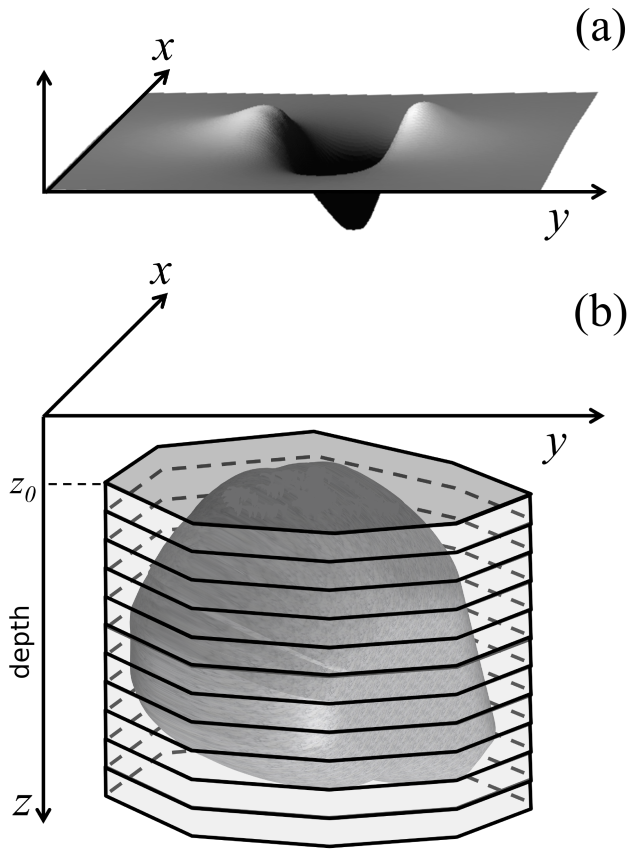

Figure 1. Schematic representation (modified from Oliveira Jr. & Barbosa (2013)) of (a) total-filed anomaly (gray surface) produced by (b) a 3-D anomalous source (dark gray volume). The interpretation model in (b) consists of a set of L vertical, juxtaposed 3-D prisms P^k , $k = 1, \ldots, L$, (light gray prisms) in the vertical direction of a right-handed coordinate system.

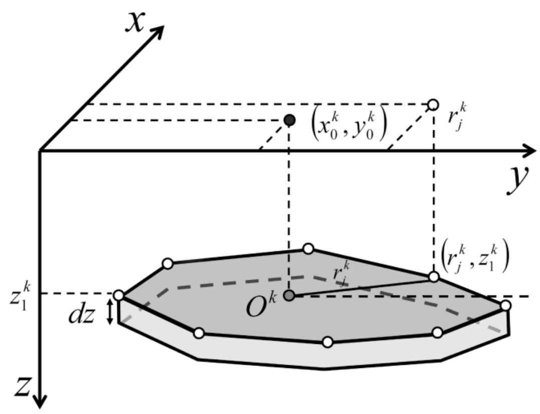

Figure 2. Polygonal cross-section of the kth vertical prism described by V vertices (white dots) with radii r_j^k, $j = 1, \ldots, V$, $k = 1, \ldots, L$, referred to an arbitrary origin O^k (grey dot) with horizontal Cartesian coordinates $(x_0^k\ , y_0^k)$, $k = 1, \ldots, L$, (black dot).

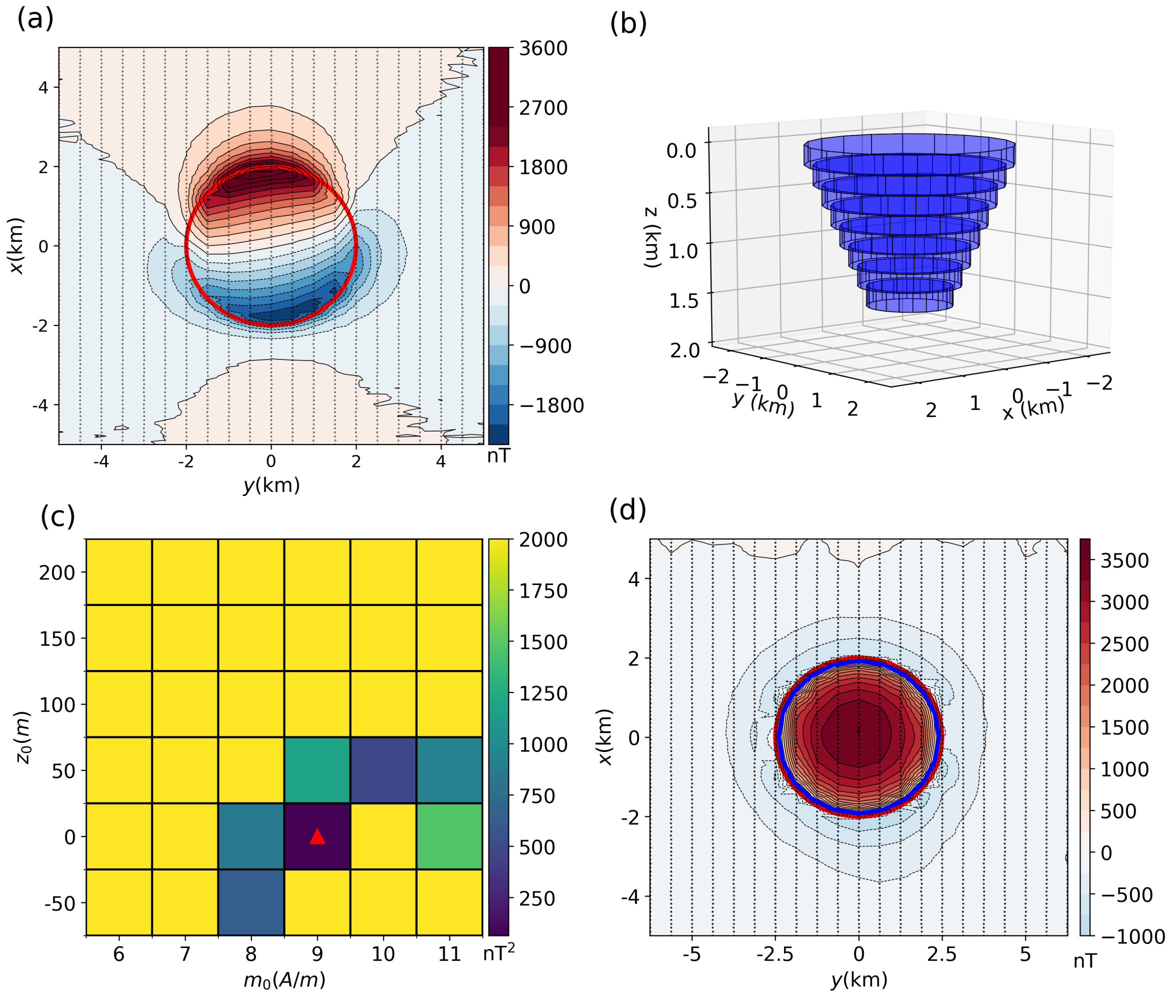

Figure 3. Simple model simulation. (a) Noise-corrupted total-field anomaly produced by the lopolithic-like body (blue prisms) shown in the panel (b). The black dots represent the observation points. The connected red dots represent the horizontal projection of the initial approximation $\hat{\mathbf{p}}_{(0)}$ (red prisms in Fig. 4b). (b) Perspective view of the simple model (lopolithic intrusion) represented by the blue prisms.

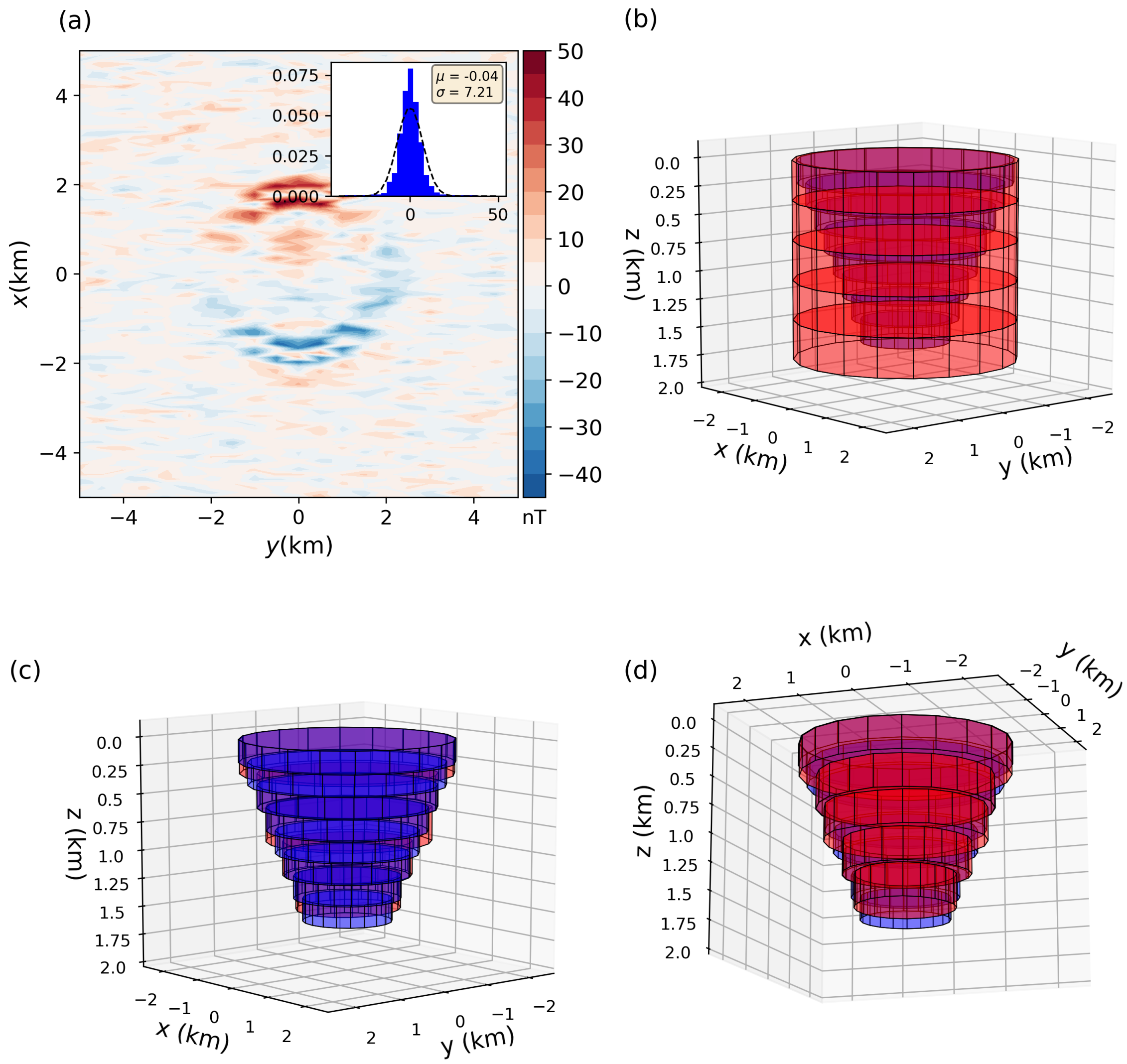

Figure 4. Simple model data. (a) Residuals between the noise-corrupted data (Fig. 3a) and the predicted data (not shown) produced by the estimated model (red prisms shown in the panels c and d). The inset in (a) shows the histogram of the residuals and the Gaussian curve (dashed line) has mean and standard deviation equal to $\mu = -0.04$ nT and $\sigma = 7.21$ nT, respectively. (b) Perspective views of the initial approximation (red prisms) and the true model (blue prisms). (c) and (d) Comparison between the estimated source (red prisms) and the true model (blue prisms) in perspective views.

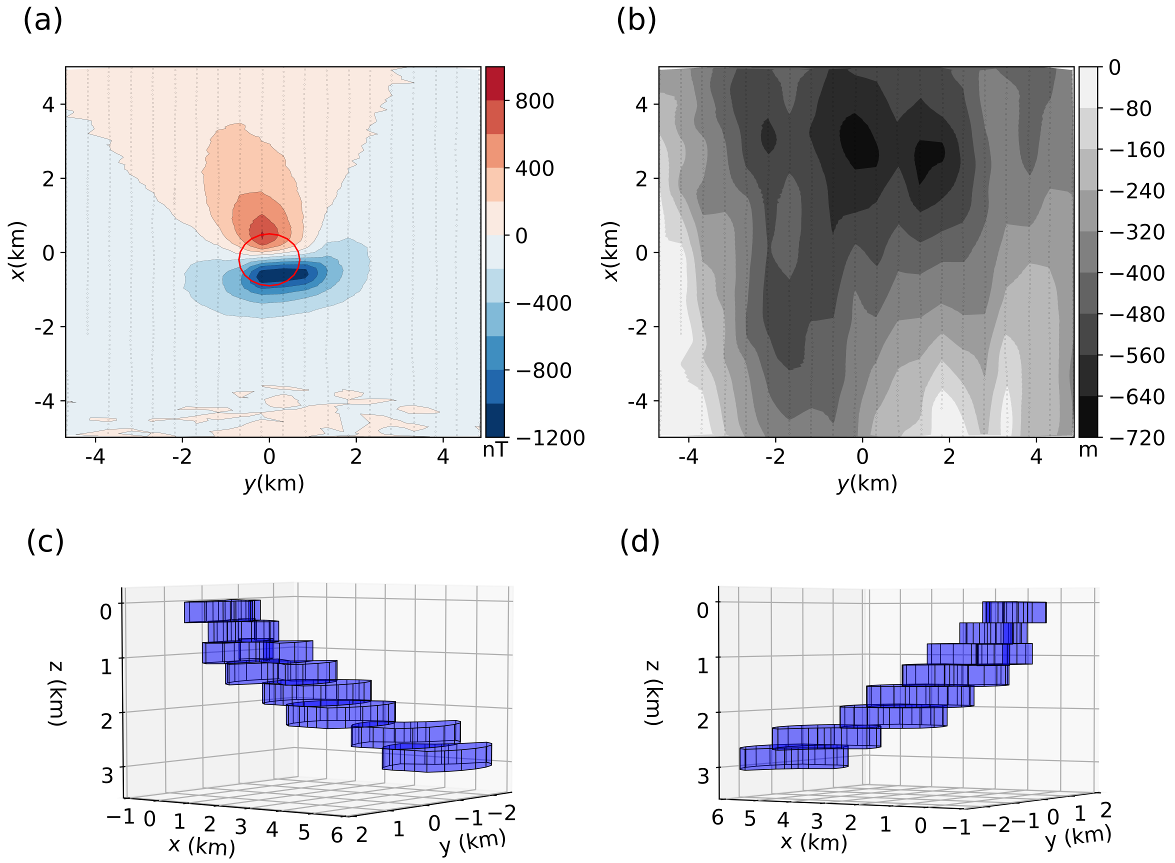

Figure 5. Dipping model simulation. (a) Noise-corrupted total-field anomaly produced by the dipping model (blue prisms shown in the panels c and d). The black dots represent the observation points. The connected red dots represent the horizontal projection of the initial approximation $\hat{\mathbf{p}}_{(0)}$ (red prisms in Fig. XXXXX. (b) Vertical coordinates of the observations simulating an airborne survey. (c) and (d) Perspective views of the dipping model represented by the blue prisms.

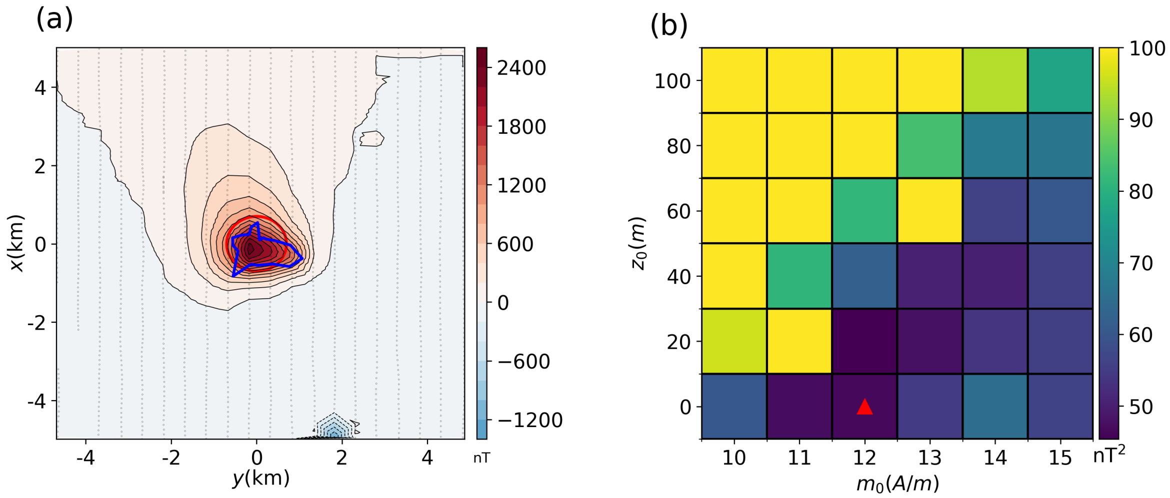

Figure 6. Dipping model simulation. (a) RTP anomaly of the total-field anomaly shown in Fig. 5a. (b)Discrete mapping of the goal function (eq. 4) produced by the estimates obtained considering a grid of 6 × 6 tentative values of depth to the top z_0 and total-magnetization intensity m_0. The red triangle and white diamond pinpoint, respectively, the true and retrieved values of m_0 and z_0.

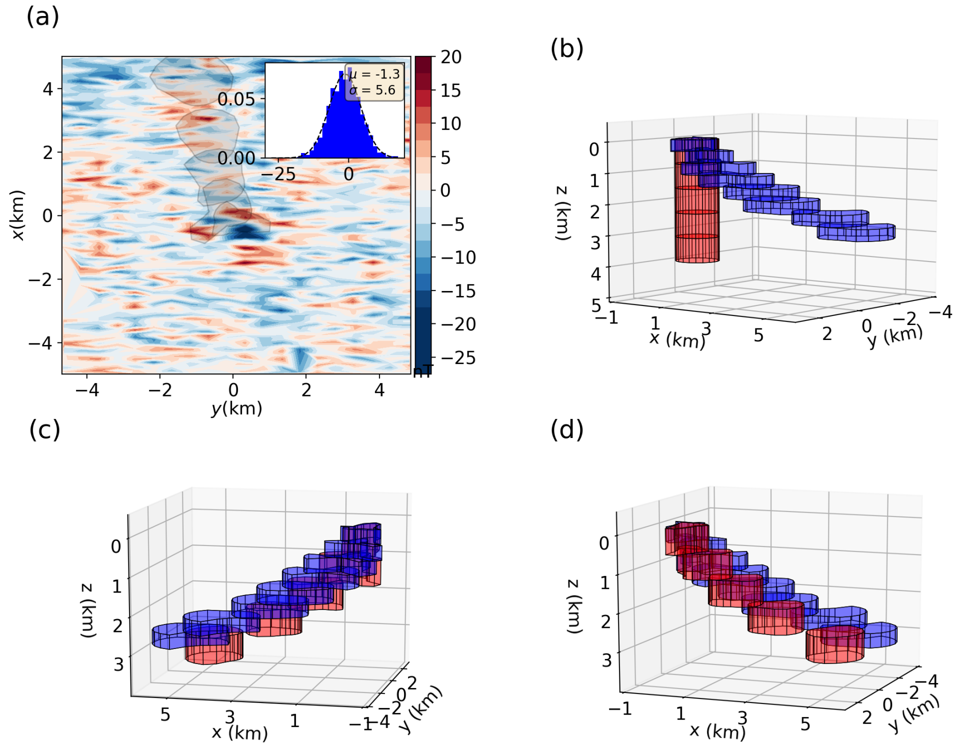

Figure 7. Dipping model simulation. (a) Residuals between the noise-corrupted data (Fig. 5a) and the predicted data (not shown) produced by the estimated model (red prisms shown in the panels c and d). The inset in (a) shows the histogram of the residuals and the Gaussian curve (dashed line) has mean and standard deviation equal to $\mu = 1.3$ nT and $\sigma = 5.6$ nT, respectively. (b) Perspective views of the initial approximation (red prisms) and the true model (blue prisms). (c) and (d) Comparison between the estimated source (red prisms) and the true model (blue prisms) in perspective views.

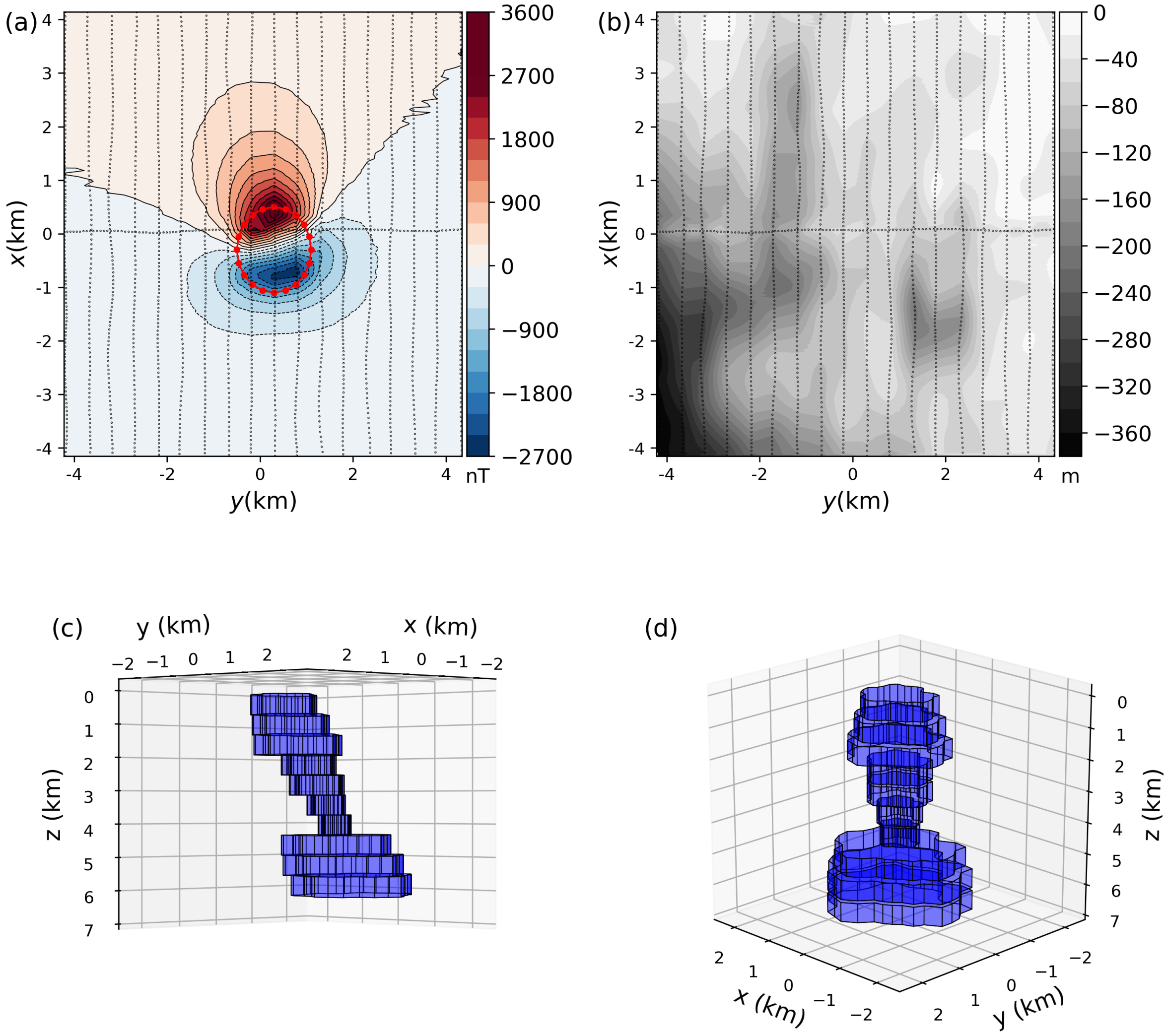

Figure 8. Complex model simulation. (a) Noise-corrupted total-field anomaly produced by the complex model (blue prisms shown in the panels c and d). The black dots represent the observation points. The connected red dots represent the horizontal projection of the initial approximation $\hat{\mathbf{p}}_{(0)}$ (red prisms in Fig. 9b). (b) Vertical coordinates of the observations simulating an airborne survey. (c) and (d) Perspective views of the complex model represented by the blue prisms.

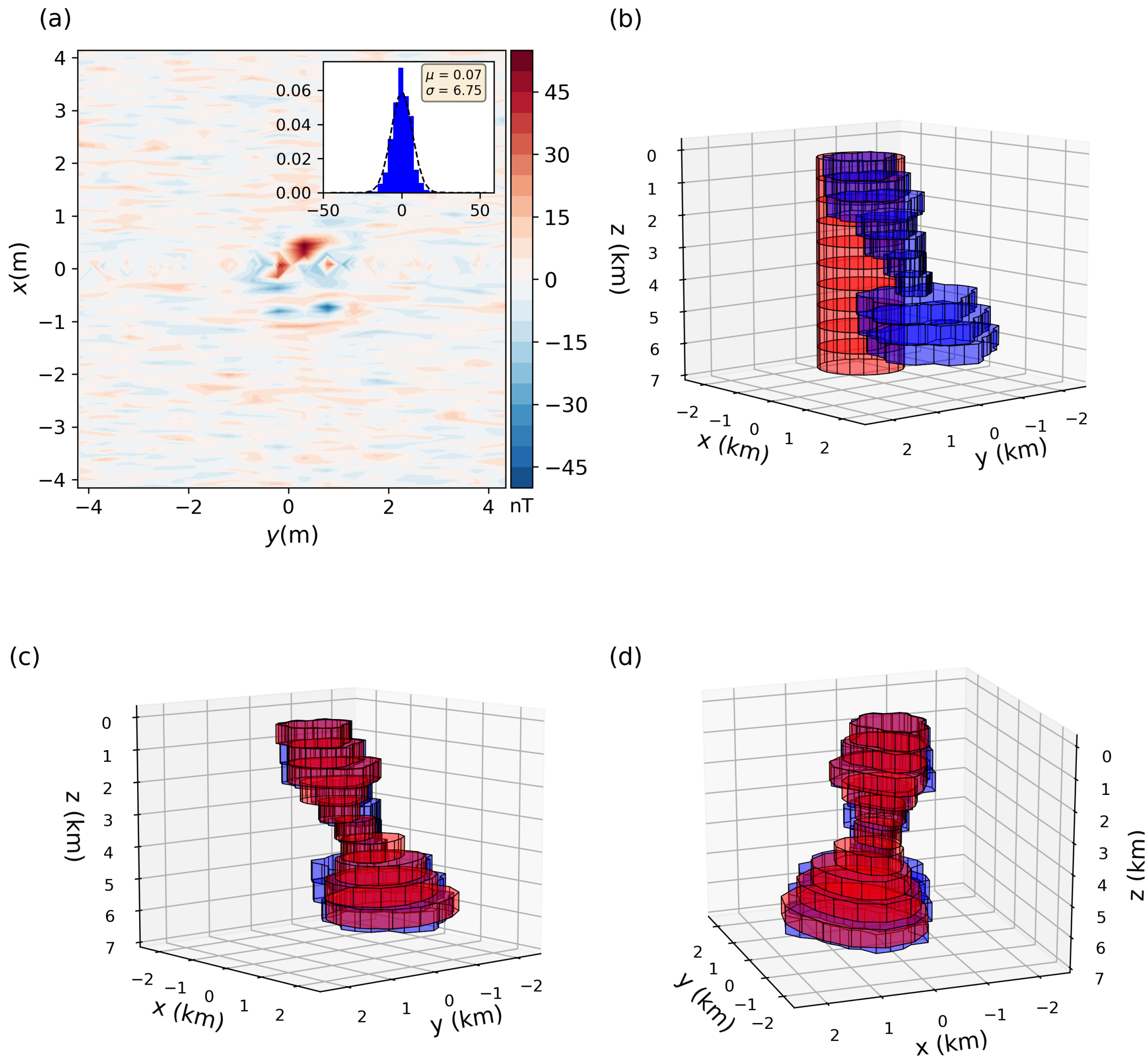

Figure 9. Application to complex model data. (a) Residuals between the noise-corrupted data (Fig. 8a) and the predicted data (not shown) produced by the estimated model (red prisms in the c and d panels). This model was obtained with the values of m_0 and z_0 represented by the white diamond in Fig. **??**. The inset in (a) shows the histogram of the residuals and the fitted Gaussian curve (dashed line) with mean and standard deviation equal to $\mu = 0.07$ nT and $\sigma = 6.75$ nT, respectively. (b) Perspective view of the initial approximation (red prisms) and the true model (blue prisms). (c) and (d) Comparison between the estimated source (red prisms) and the true model (blue prisms) in perspective views.

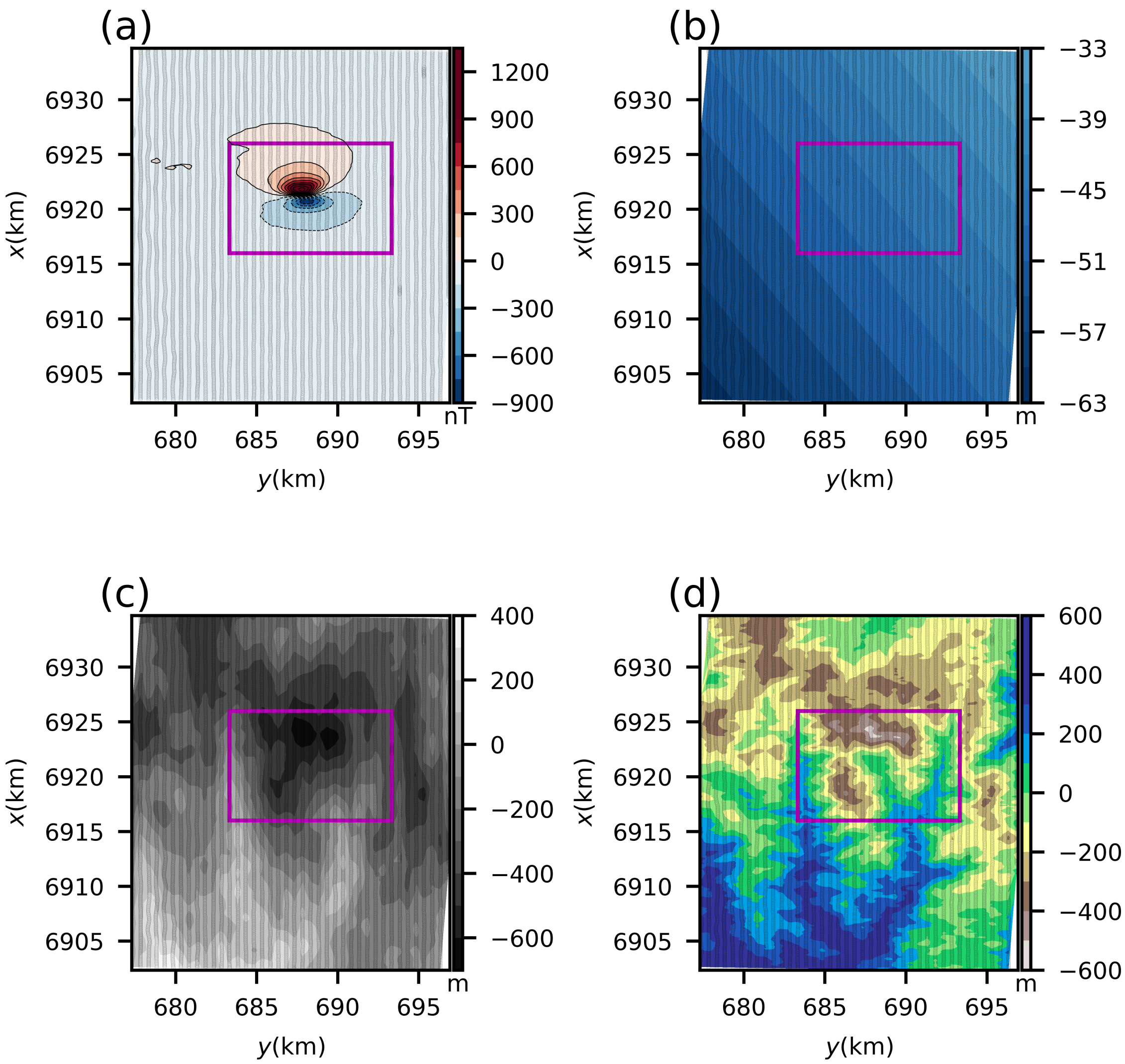

Figure 10. (a) Residual total-field anomaly (in nT) over the Anitápolis complex in southern Brazil. The horizontal UTM coordinates are referred to the central meridian 51° W. (b) Geometric height of the observation points and (c) topography of the study area. Both of them are referred to the WGS84 ellipsoid. For convenience, we have subtracted 800 m from their values. The black dots represent the observation points. The connected red dots represent the horizontal projection of the initial approximation $\hat{\mathbf{p}}_{(0)}$ (red prisms in Figs 11b and 12b).

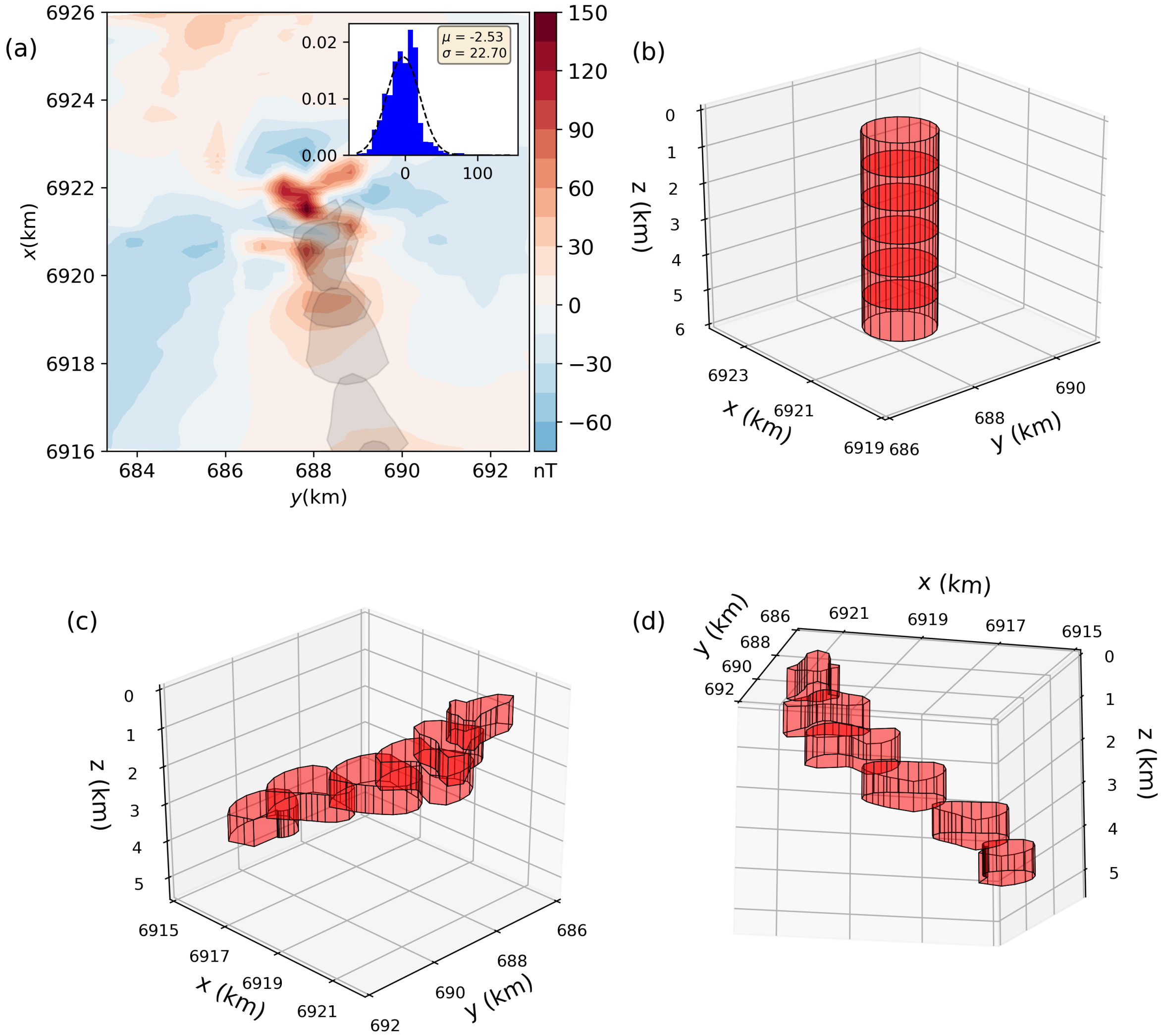

Figure 11. Application to the field data over the Anitápolis complex, Brazil. The non-outcropping estimated model producing the smallest goal function value, represented by the pink diamond in Fig. **??**. (a) Residuals between the observed data (Fig. 10a) and the predicted data (not shown) produced by the estimated model. The inset shows the histogram of the residuals and the fitted normal Gaussian curve (dashed line) with mean $\mu = -2.53$ nT and standard deviation $\sigma = 22.70$ nT. The light-gray polygons represent the horizontal projection of the estimated model onto the residual map. (b) Perspective view of the initial approximation (red prisms). (c) and (d) Perspective views of the estimated model (red prisms).

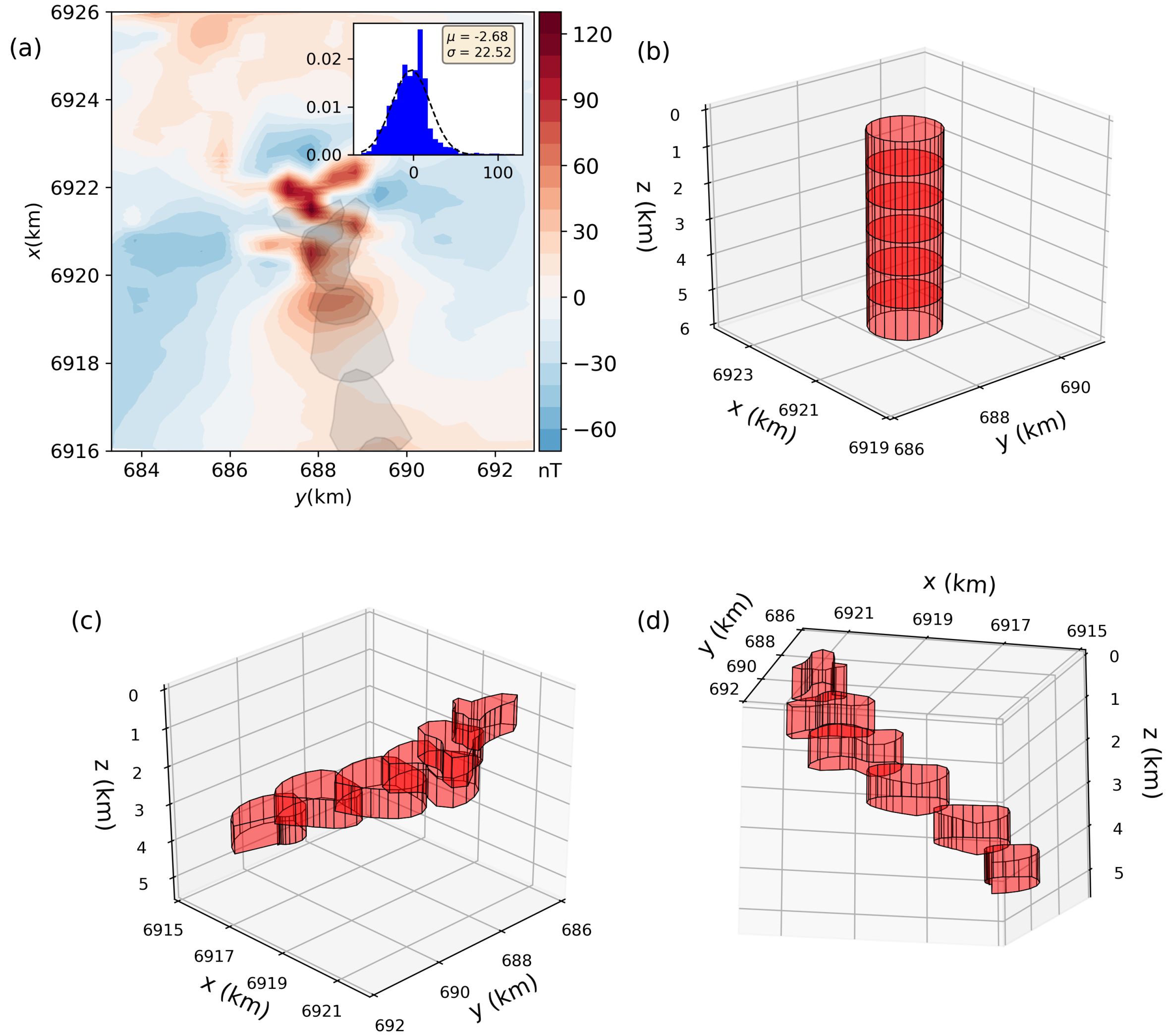

Figure 12. Application to the field data over the Anitápolis complex, Brazil. Outcropping estimated model represented by the white diamond in Fig. **??**. (a) Residuals between the observed data (Fig. 10a) and the predicted data (not shown) produced by the estimated model. The inset shows the histogram of the residuals and the fitted normal Gaussian curve (dashed line) with mean $\mu = -2.68$ and standard deviation $\sigma = 22.52$. The light-gray polygons represent the horizontal projection of the estimated model onto the residual map. (b) Perspective view of the initial approximation (red prisms). (c) and (d) Perspective views of the estimated model (red prisms).